J. Fluid Mech. (2008), *vol.* 599, *pp.* 51–79. © 2008 Cambridge University Press
doi:10.1017/S0022112007009354 Printed in the United Kingdom

Intermittent turbulence in a pulsating pipe flow

RAFFAELLA TUZI† AND PAOLO BLONDEAUX
Department of Environmental Engineering, University of Genoa, Via Montallegro 1, 16145 Genoa, Italy

(Received 7 November 2006 and in revised form 26 September 2007)

Numerical simulations of the pulsating flow in a pipe of circular cross-section characterized by small imperfections are carried out to determine the conditions leading to the appearance of turbulence. The results show that in the oscillatory case (no steady velocity component of the basic flow), the critical value of the Reynolds number R_δ depends on the Womersley parameter α and, in particular, R_δ increases as α decreases. The critical value of R_δ of the plane wall case is recovered when α is larger than about 10. For moderate values of the Reynolds numbers but larger than the critical one, turbulence appears around flow reversal and breaks the symmetry of the flow, originating a steady velocity component. Moreover, turbulence is not present throughout the whole cycle and there are phases during which the flow relaminarizes. The presence of a steady pressure gradient tends to destabilize the flow and this destabilizing effect becomes larger as the steady velocity component is increased. When turbulence is present, its dynamics is similar to that of the steady case and a log-law layer can be identified both in the oscillatory and the pulsating case.

1. Introduction

Even though time-periodic flows occur in many engineering applications, the interest in the study of transition and turbulence structure in pulsating flows arises mainly from the pulsating character of most physiological flows, which are often generated by peristaltic pumps.

Using visual observations and measurements of the instantaneous velocity profiles, Nerem, Seed & Wood (1972) performed a detailed study of the flow in the thoracic aorta of dogs and distinguished different flow regimes. Those with negligible high-frequency velocity oscillations were assumed to represent a laminar flow. Those characterized by high-frequency velocity oscillations present only during a small part of the cycle, i.e. at the peak systolic phase, were thought to represent a transitional condition. Finally, the velocity profiles with high-frequency oscillations persisting throughout the decelerating phase of systole were thought to be representative of the turbulent regime, even though turbulence was damped out during the diastolic phase. Ojha *et al.* (1989), addressing phenomena encountered in mild stenoses of medium-sized arteries, studied a pulsatile flow through constricted tubes and found vortical and helical structures which were formed primarily during the decelerating phase of the cycle and near the reattachment point downstream of the constriction. Under some conditions, they observed transition to turbulence, accompanied by intense fluctuations of the wall shear stress.

---

† Present address: DLR, German Aerospace Center Institute of Aerodynamics and Flow Technology, Bunsenstrasse 10, 37073 Göttingen, Germany.

Even though there is evidence that turbulence may also be present in healthy subjects, traditionally it is assumed that a turbulent flow in the human circulatory system is generally evidence of a disorder, such as a valvular stenosis, and may be detected as 'murmurs' via a stethoscope (Leon & Shaver 1974).

Also, the respiratory flow in the small airways can be regarded as an oscillatory flow in a pipe and the basic mechanisms associated with human speech can be modelled as a pulsatile flow through a pipe with a constriction formed by the vocal folds, followed by an abrupt area expansion. In acoustics, it is well known that there is a strong interaction between turbulence and separation phenomena (Hirschberg, Gilbert & Wijnands 1996). Turbulence tends to destroy the coherent, long-lasting vortical structures generated by flow separation.

Hence, it is important to determine the conditions leading to the appearance of turbulence and to understand the mechanism of turbulence production in a time-periodic flow.

Though a complex geometry is usually associated with physiological flows (curvature of the pipe axis, bifurcations, narrowing and widening of the cross-section, etc.), a first step in understading transition to turbulence is the study of transition in a straight tube of constant circular cross-section. A deep understanding of the instability mechanism and of the flow structure in this simple geometry may lead to a better understanding of the transport phenomena even in complex geometries.

However, less is known about transition in a pulsatile flow in a pipe of circular cross-section. Attention has been mainly focused on flat Stokes boundary layers. Von Kerczek & Davis (1974) and Hall (1978), using a 'global' instability criterion based on Floquet theory, found that the flow was stable within the investigated range of the Reynolds number. Von Kerczek & Davis (1974) and Blondeaux & Seminara (1979), using a 'momentary' criterion for instability, found that for Reynolds numbers larger than a critical value there are parts of the cycle near flow reversal during which the flow is unstable. However, after a cycle, the perturbations experience a net decay. Akhavan *et al.* (1991*b*) showed that three-dimensional disturbances can experience a net growth when interacting with pre-existing finite-amplitude two-dimensional waves which, according to Blondeaux & Vittori (1994), can be generated by the resonant interaction of the oscillatory Stokes flow with wall imperfections. More recently, Blennerhassett & Bassom (2002), by means of a linear stability analysis based on Floquet theory, have predicted that the flat Stokes layer is unstable for Reynolds numbers larger than 1416. Hereafter, the Reynolds number is defined as $R_\delta = U_0^* \delta^* / \nu^*$ (U_0^* is the amplitude of the velocity oscillations far from the wall, $\delta^* = \sqrt{2\nu^*/\omega^*}$ is the thickness of the viscous Stokes layer, ν^* is the kinematic viscosity of the fluid and ω^* is the angular frequency of the fluid oscillations). Moreover, Blennerhassett & Bassom (2006) have shown that the oscillatory flow in a two-dimensional channel has essentially the same critical conditions for instability as the semi-infinite Stokes layer flow, provided that the channel width is larger than $28\delta^*$.

Instability of a sinusoidally modulated pipe flow with zero mean has been investigated experimentally by, among others, Sergeev (1966), Merkli & Thomann (1975), Hino, Sawamoto & Takasu (1976), Eckmann & Grotberg (1991). On the basis of the experimental measurements, four different flow regimes can be identified: (*a*) the laminar regime, (*b*) the flow regime where 'small-amplitude' perturbations appear superimposed on the Stokes flow but the average velocity profiles exhibit only small deviations from the laminar case, (*c*) the flow regime where bursts of turbulence appear only during the decelerating phases of the cycle, (*d*) the flow regime characterized by the presence of turbulence throughout the whole cycle. Different names have been used in the literature to identify these four regimes. For the sake of clarity, we follow Blondeaux & Vittori (1994) and identify regime (*b*) as the 'disturbed laminar' regime, regime (*c*) as the 'intermittently turbulent' regime and regime (*d*) as the 'fully turbulent' regime.

In more detail, Tromans (1976) found a critical value of the Reynolds number for the onset of instability equal to 130 and a value equal to 500 above which he observed turbulence which, however, appeared only during the decelerating phases, while in the accelerating phases the flow recovered a laminar behaviour. Hino *et al.* (1976) found that disturbances of the laminar flow first appeared when the Reynolds number R_δ fell in the range 70–550 depending on the Womersley parameter $\alpha = R^*/\delta^*$ (R^* is the pipe radius), provided α was not too small. However, Hino *et al.* (1976) found that the velocity profiles exhibited only small deviations from the laminar case. On the contrary when the Reynolds number exceeded 550, for every value of α except for very small values, the velocity profiles were disturbed by much larger fluctuations. More recently, Eckmann & Grotberg (1991) performed some experiments for $6.36 < \alpha < 23.33$. They detected transition to turbulence at R_δ equal to 500 and found turbulence only during the decelerating phases. Lodhal, Sumer & Fredsøe (1998) defined turbulence as occurring when there was any sign of imperfection in the wall shear stress signal and found that the critical value of the Reynolds number depends on the parameter α. In particular, this critical value is about 500 when α is larger than 10 but it increases when α is decreased (see figure 3 of Lodhal *et al.* 1998). For example, for $\alpha = 25$ and 53, the critical value of the Reynolds number is about 550, but for $\alpha = 4.2$ it about 900 and for $\alpha = 3.3$ it becomes 2000. Monkewitz (1983) observed that the laminar Stokes profile showed no significant distortion up to values of the Reynolds number of approximately 500. Moreover, he found that a vortical disturbance appeared very clearly at a Reynolds number equal to 647 just before flow reversal. Akhavan *et al.* (1991*a*) conducted experiments for Reynolds numbers in the range 550–2000 and for Womersley parameters in the range 5–10. In all the investigated flows, turbulence appeared toward the end of the accelerating phases of the cycle and was sustained throughout the decelerating phases. During the turbulent portion of the cycle, production of turbulence was restricted to the wall region and was the result of turbulent bursts. Moreover, the three-layer description of the flow consisting of a viscous sublayer, a logarithmic layer (with von Kármán constant equal to 0.4) and an outer wake was identified.

From this brief summary of the experimental results, it appears that transition from the laminar to the disturbed laminar regime (regime (*b*)) is quite sensitive to the particular experimental set-up (some authors observed a direct transition from the laminar regime to the intermittently turbulent one) and the critical value of the Reynolds number depends on the Womersley parameter α (Hino *et al.* 1976). Transition to the 'intermittently turbulent' regime is usually well defined and mainly independent of the particular experimental set-up; however, the critical value of the Reynolds number for transition from regime (*b*) to regime (*c*) is found to be independent of α by Hino *et al.* (1976) while the results of Lodhal *et al.* (1998) suggest that it depends on α.

Instability of a periodic pipe flow with a non-zero mean flow has been investigated by, among others, Gilbrech & Combs (1963), Sarpkaya (1966), Yellin (1966). The phenomenon has been experimentally studied by Stettler & Hussain (1986) who determined the transition limits in the three-dimensional parameter space defined by the mean and modulation Reynolds numbers and by a frequency parameter. In particular, Stettler & Hussain (1986) focused their attention on the structure of the observed turbulent patches, which differed in structural detail from the turbulent puffs or slugs normally seen in steady flows. A more recent investigation has been carried out by Lodhal *et al.* (1998). The results of figure 6 of their paper show that a steady pipe flow is stabilized by the superposition of weak velocity oscillations for any value of the Womersley parameter. However, strong velocity oscillations are able to trigger turbulence even when the steady flow should be in the laminar regime and this destabilizing effect becomes larger when the parameter α is increased. Moreover, the measurements by Lodhal *et al.* (1998) in the oscillatory-dominated case (large values of the velocity oscillations and a small steady current) show that turbulence is mainly confined to the decelerating phases of the cycle and the flow tends to relaminarize during the accelerating phases. Some works have been devoted to the study of the effects of the flow modulation on turbulence structure at moderate Reynolds numbers (e.g. Shemer, Wygnanski & Kit 1985; Ramaprian & Tu 1980). Even though interesting results have been obtained, further investigations are still required to have a complete picture of the phenomenon.

Here, the transitional pulsating flow in a pipe is investigated by means of numerical simulations. The main goal of the present study is the determination of the critical conditions and the identification of the mechanism that leads to turbulence.

The rest of the paper is organized as follows. In the next section we formulate the problem and briefly describe the numerical approach used to integrate the Navier–Stokes and continuity equations. In § 3, we describe the results, focusing our attention on the values of the parameters which give rise to a turbulent flow. The final section is devoted to the conclusions and to a description of future research.

2. Formulation of the problem and numerical approach

The pulsatile flow of a viscous incompressible homogeneous fluid in a pipe of circular cross-section is considered. The kinematic viscosity and the density of the fluid are denoted by ν^* and ρ^*, respectively. A cylindrical coordinate system (x^*, r^*, θ) is introduced, such that the x^*-axis coincides with the pipe axis and the surface $r^* = R^*$ describes the average position of the pipe wall. A star denotes a dimensional quantity, while the same symbol without the star denotes its dimensionless counterpart. The flow is driven by a pressure gradient, along the pipe axis, such that

$$\left(\frac{\partial p^*}{\partial x^*}, \frac{\partial p^*}{\partial r^*}, \frac{1}{r^*}\frac{\partial p^*}{\partial \theta}\right) = \left[G_s^* + \left(\frac{G_o^*}{2}\mathrm{e}^{\mathrm{i}\omega^* t^*} + \mathrm{c.c.}\right), 0, 0\right] \tag{2.1}$$

where p^* denotes the pressure, t^* is the time, ω^* is the angular frequency of the pressure oscillations and G_s^*, G_o^* are given constants.

As in Blondeaux & Vittori (1994), Verzicco & Vittori (1996), Vittori & Verzicco (1998) and Costamagna, Vittori & Blondeaux (2003), the pipe walls are not perfectly flat but small imperfections are introduced such that the wall profile is given by the superimposition of different sinusoidal components,

$$r^* = R^* + \epsilon^* \sum_{n=1}^{N} a_n \cos(\alpha_n^* x^* + \gamma_n \theta + \varphi_n) = R^* + \epsilon^* \eta(x^*, \theta), \tag{2.2}$$

where $\epsilon^* a_n$ denotes the amplitude of the nth component which is characterized by wavenumbers α_n^* and γ_n in the x^*- and θ-directions respectively and by a phase φ_n. If no wall imperfection is introduced, transition can be triggered only by inserting quite large perturbations (Spalart & Baldwin 1987; Akhavan *et al.* 1991*b*) and turbulence appears for Reynolds numbers larger than those observed during the laboratory experiments. On the other hand, a small wall waviness is able to produce a large response, which is related to a receptivity mechanism which is present both in steady and unsteady flow (see Luo & Wu 2004; Wu & Luo 2006; Luchini & Bottaro 2001). Moreover, the numerical simulations show that small wall imperfections induce significant perturbations of the laminar flow in a range of the Reynolds number for which the disturbed laminar flow is experimentally observed. Turbulence is triggered when the Reynolds number is larger than a critical value, which agrees well with experimental observations (Verzicco & Vittori 1996; Vittori & Verzicco 1998). Note that, having in mind physiological flows and fixing $\nu^* = 10^{-6}\,\mathrm{m^2\,s^{-1}}$, $\omega^* = 6.28$ Hz, the values of ϵ^* used in the numerical simulations are such that the amplitude of the wall imperfections is of order 10^{-3} mm.

In the laminar regime the velocity field is unidirectional and the solution of the problem posed by the Navier–Stokes and continuity equations can be easily determined:

$$(u^*, v^*, w^*) = \left[U_s^* f(r^*) + \left(\frac{U_o^*}{2} g(r^*) \mathrm{e}^{\mathrm{i}\omega^* t^*} + \text{c.c.}\right), 0, 0\right] + O(\epsilon), \tag{2.3}$$

where (u^*, v^*, w^*) denote the three velocity components along the (x^*, r^*, θ)-axes respectively, U_s^* is the maximum velocity induced by the steady component of the pressure gradient,

$$U_s^* = -\frac{G_s^* R^{*2}}{4\mu^*}, \tag{2.4}$$

U_o^* is a complex quantity describing the amplitude and phase of the velocity oscillations induced by the oscillating pressure gradient,

$$U_o^* = -\frac{\mathrm{i}G_o^*}{\rho^*\omega^*}\left[\frac{1}{J_0\left[(-1+\mathrm{i})R^*/\delta^*\right]} - 1\right], \tag{2.5}$$

and $f(r^*)$ and $g(r^*)$ are functions of the radial coordinate which describe the velocity profiles,

$$f(r^*) = 1 - \frac{r^{*2}}{R^{*2}}, \tag{2.6}$$

$$g(r^*) = \frac{J_0\left[(-1+\mathrm{i})r^*/\delta^*\right] - J_0\left[(-1+\mathrm{i})R^*/\delta^*\right]}{1 - J_0\left[(-1+\mathrm{i})R^*/\delta^*\right]}. \tag{2.7}$$

In (2.5), (2.7) J_0 denotes the Bessel function of the first kind of zero order. In particular, the form of the solution depends on the ratio between G_s^* and G_o^* and on the dimensionless parameter

$$\alpha = \frac{R^*}{\delta^*} \tag{2.8}$$

which is the Womersley number, also called frequency parameter (Sarpkaya 1966) or Stokes number (Goldschmied 1970). When G_o^* vanishes, steady Poiseuille flow is found. On the other hand, when G_s^* vanishes an oscillatory flow with a vanishing time average is forced. While the velocity profile of the steady velocity component turns out to be parabolic, the velocity profile of the oscillatory velocity component depends on the dimensionless parameter α. In figure 1 the velocity profile u^*/U_0^* is shown at different phases of the cycle for $\alpha = 4, 8, 32$ and $G_s^*/G_o^* = 0$. If α is much larger than one, a plug flow is generated and viscous effects are confined close to wall in a boundary layer, the thickness of which is much smaller than the radius of the pipe. Moreover,

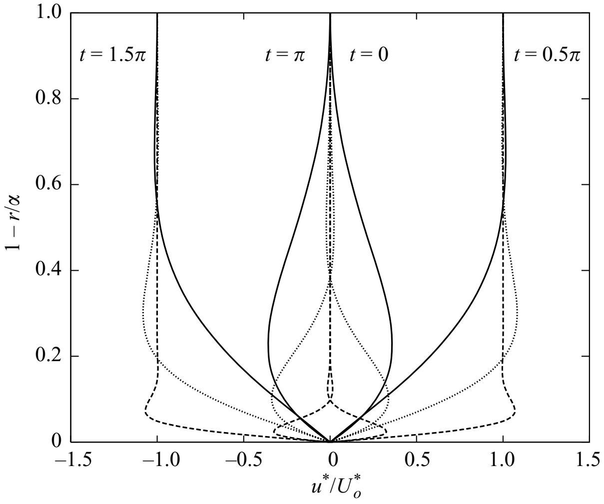

FIGURE 1. Velocity profiles u^*/U_o^* at different phases of the cycle for $\alpha = 4$ (solid lines), $\alpha = 8$ (dotted lines), $\alpha = 32$ (short-dashed lines).

the velocity oscillations are out of phase with the oscillations of the pressure gradient. In this case U_o^* tends to $-(\mathrm{i}G_o^*)/(\omega^* \rho^*)$ and $g(r^*)$, far from the wall, tends to 1.

Beside the parameters α and G_s^*/G_o^* (or alternatively U_s^*/U_o^*), the flow is controlled by a typical Reynolds number which can be defined by either using the steady velocity component or the oscillating one. Hereafter, we choose the second one and we define the Reynolds number R_δ as

$$R_\delta = \frac{\hat{U}_o^* \delta^*}{\nu^*} \tag{2.9}$$

where $\hat{U}_o^* = |U_o^*|$ is the amplitude of the velocity oscillations along the pipe axis. The Reynolds numbers $Re = \hat{U}_o^* R^*/\nu^*$ and $RE = \hat{U}_o^{*2}/\nu^* \omega^*$, used by other investigators, are simply αR_δ and $R_\delta^2/2$, respectively. As described in the introduction, the laminar flow described by (2.3)–(2.7) is found when the Reynolds number R_δ is smaller than a first critical value. For larger values of R_δ but smaller than a second critical value, disturbances start to appear but the mean flow deviates from the solution (2.3) only slightly. Only when R_δ is larger than the second critical value, is turbulence triggered. When flow disturbances start to appear and the flow departs from laminar behaviour, the growth of perturbations and the process which leads the flow to the turbulent regime can be studied by performing numerical simulations of the Navier–Stokes and continuity equations. The problem is written in dimensionless form using δ^* as length scale, $(\omega^*)^{-1}$ as time scale, $\hat{U}_o^*$ as velocity scale and $\rho^* \hat{U}_o^{*2}$ as scale for the pressure. This choice has been made since we focus our attention on cases always characterized by significant values of the velocity oscillations. The continuity and momentum equations become

$$\frac{\partial u}{\partial x} + \frac{1}{r}\frac{\partial (rv)}{\partial r} + \frac{1}{r}\frac{\partial w}{\partial \theta} = 0, \tag{2.10}$$

$$\frac{\partial u}{\partial t} + \frac{R_\delta}{2}\left[u\frac{\partial u}{\partial x} + v\frac{\partial u}{\partial r} + \frac{w}{r}\frac{\partial u}{\partial \theta}\right] = -\frac{R_\delta}{2}\left[\frac{\partial p}{\partial x} + G_s + \left(\frac{G_o}{2}\mathrm{e}^{it} + \text{c.c.}\right)\right] + \frac{1}{2}\left[\frac{\partial^2 u}{\partial x^2} + \frac{1}{r}\frac{\partial}{\partial r}\left(r\frac{\partial u}{\partial r}\right) + \frac{1}{r^2}\frac{\partial^2 u}{\partial \theta^2}\right], \tag{2.11}$$

$$\frac{\partial v}{\partial t}+\frac{R_\delta}{2}\left[u\frac{\partial v}{\partial x}+v\frac{\partial v}{\partial r}+\frac{w}{r}\frac{\partial v}{\partial \theta}-\frac{w^2}{r}\right]=-\frac{R_\delta}{2}\frac{\partial p}{\partial r}+\frac{1}{2}\left[\frac{\partial^2 v}{\partial x^2}+\frac{1}{r}\frac{\partial}{\partial r}\left(r\frac{\partial v}{\partial r}\right)\right.$$
$$\left.+\frac{1}{r^2}\frac{\partial^2 v}{\partial \theta^2}-\frac{v}{r^2}-\frac{2}{r^2}\frac{\partial w}{\partial \theta}\right], \qquad (2.12)$$

$$\frac{\partial w}{\partial t}+\frac{R_\delta}{2}\left[u\frac{\partial w}{\partial x}+v\frac{\partial w}{\partial r}+\frac{w}{r}\frac{\partial w}{\partial \theta}+\frac{vw}{r}\right]=-\frac{R_\delta}{2}\frac{1}{r}\frac{\partial p}{\partial \theta}+\frac{1}{2}\left[\frac{\partial^2 w}{\partial x^2}+\frac{1}{r}\frac{\partial}{\partial r}\left(r\frac{\partial w}{\partial r}\right)\right.$$
$$\left.+\frac{1}{r^2}\frac{\partial^2 w}{\partial^2 \theta}+\frac{2}{r^2}\frac{\partial v}{\partial \theta}-\frac{w}{r^2}\right], \qquad (2.13)$$

where (u, v, w) are the axial, radial and azimuthal velocity components, respectively. The problem is closed by the no-slip boundary condition

$$(u, v, w)=0 \quad \text{at} \quad r=\alpha+\epsilon\eta(x, \theta). \qquad (2.14)$$

The solution of the problem is determined numerically with a finite difference approach using the laminar velocity field (2.3) as initial condition. Standard centred second-order finite difference approximations of the spatial derivatives are used. The time-advancement of the Navier–Stokes equation employs a fractional-step method extensively described by Kim & Moin (1985), Orlandi (2000) and Rai & Moin (1991). The non-solenoidal intermediate velocity field is evaluated by means of a third-order Runge–Kutta scheme to discretize convective terms together with a Crank–Nicholson scheme for the diffusive terms. The implicit treatment of the viscous terms would require the inversion of large sparse matrices, which are reduced to tridiagonal matrices by a factorization procedure with an error of order $(\Delta t)^3$ (Beam & Warming 1976). Then, by enforcing the continuity equation, a Poisson equation for the pressure field is obtained which is readily solved by taking advantage of the imposed periodicity in the x- and θ-directions. More details on the numerical approach can be found in Tuzi (2006).

The equations are solved in a computational domain of size L_x in the streamwise direction. Since turbulence is assumed to be homogeneous along the pipe, periodic boundary conditions are enforced along the x-direction, assuming that L_x is large enough. Having assumed the amplitude of the wall waviness to be much smaller than the thickness of the laminar boundary layer ($\epsilon=\epsilon^*/\delta^* \ll 1$), the boundary condition (2.14) can be approximated as

$$(u, v, w)=-\epsilon\eta(x, \theta)\frac{\partial(u, v, w)}{\partial r}+O(\epsilon^2) \quad \text{at} \quad r=\alpha. \qquad (2.15)$$

Note that (2.15) is an approximation of the boundary condition (2.14) within the accuracy of the numerical method employed to solve (2.10)–(2.13). The numerical scheme is second-order accurate in space and in all the simulations ϵ has been taken to be smaller than the size of the first computational cell close to the wall. In the computer code, the variables $(q_x, q_r, q_\theta)=(u, rv, rw)$ are introduced in such a way that at $r=0$ only the boundary condition $q_r=0$ needs to be forced (Orlandi 2000).

The use of periodic boundary conditions in the homogeneous direction is justified if the computational box is large enough to include the largest eddies in the flow. The results of Blondeaux & Seminara (1979), Akhavan *et al.* (1991*b*), Wu (1992), Blondeaux & Vittori (1994), Vittori & Verzicco (1998), and Costamagna *et al.* (2003), who investigated the plane wall case, suggest that the vortex structures, which tend to appear when transition to turbulence takes place, are characterized by a length in the streamwise direction equal to about $12.56\delta^*$. Even though differences are expected to be induced by the cylindrical geometry of the pipe and by the presence of a steady velocity component, this value provides at least the order of magnitude of the length of the most unstable perturbations. Since, as in Jimenez & Moin (1991), the goal here is to isolate the basic flow unit and to study its morphology and dynamics, we tried to keep the size of the computational box as small as possible to reproduce the process of turbulence generation. Hence, on the basis of preliminary numerical experiments, the numerical simulations have been made with a box size equal to $L_x^* = 50.24\delta^*$. For such a box size, turbulence is generated and maintained for Reynolds numbers which are in fair agreement with the experimental values. Moreover the average quantities, such as velocity, turbulence energy, and Reynolds stresses, agree fairly well with experimental measurements. An estimate of the box size in terms of wall units can be obtained using the maximum value of the shear velocity predicted on the basis of the laminar solution. Experimental data show that the maximum value of the wall shear stress in the intermittently turbulent regime is not much different from those characterizing the laminar solution. In the range of the Reynolds number investigated here, it turns out that the length of the computational box falls between about 2000 and 5000 wall units. Such values are similar to those used by Jimenez & Moin (1991) to study vortex structures in the wall layer in a steady flow. Finally, the ratio between the box size and the radius of the pipe section depends on the Womersley parameter and ranges from about 5 for $\alpha = 10$ to about 25 for $\alpha = 2$.

N_x, N_r, N_θ denote the number of grid points in the streamwise, radial and azimuthal directions respectively. The mesh is uniform in the streamwise and azimuthal directions while in the radial one a non-uniform mesh has been used to cluster the grid- points in the vicinity of the wall where velocity gradients are expected to be stronger during the phases of the cycle characterized by turbulence. Different values of N_x, N_r, N_θ have been used depending on the parameters of the simulation. For the smallest value of α ($\alpha = 3$), $N_x = 97$, $N_r = 37$ and $N_\theta = 97$, while for the largest value ($\alpha = 8$), $N_x = 97$, $N_r = 97$ and $N_\theta = 257$. Some of the simulations have been repeated with larger values to ascertain that the results do not depend on N_x, N_r and N_θ. An example of the instantaneous streamwise and azimuthal velocity spectra, averaged in the azimuthal and streamwise directions respectively, is shown in figure 2 at the phase of the cycle when turbulence appears and the smallest vortices are generated. For the generic velocity component u, the amplitudes of the harmonic components u_m, u_n, in the x- and θ-directions respectively, are defined by

$$u(x, r, \theta, t) = \sum_{m=-M}^{M} u_m(r, \theta, t) \mathrm{e}^{\mathrm{i}k_m x} = \sum_{n=-N}^{N} u_n(x, r, t) \mathrm{e}^{\mathrm{i}k_n \theta}, \tag{2.16}$$

where $k_m = 2\pi m / L_x$ and $k_n = n$. The plots of figure 2 are for $R_\delta = 6000$, $\alpha = 4$, $U_s^* / \hat{U}_o^* = 0$ and show an acceptable drop-off at high frequencies, confirming that the smallest scales are adequately resolved. Similar results have been obtained for different values of the parameters. However, the results obtained show that the box is somewhat short to adequately represent all turbulence characteristics: after averaging $|u_n|$ in the x-direction, the computed spectra display some small random oscillations which are due to the limited size of the box compared with the largest vortex structures. A similar problem was faced by Jimenez & Moin (1991), who circumvented it by performing the time average of spatially averaged quantities. In the present work, a phase-average value could be introduced. However, in the investigated range of the Reynolds number, turbulence appears at different instants within the cycle and a phase-average procedure would have implied averaging flow fields with different characteristics. Hence, in the following, no phase-average procedure is used.

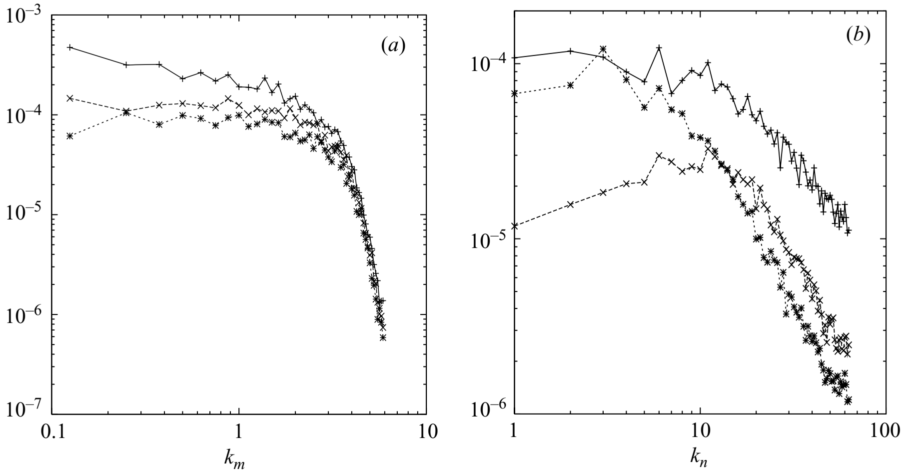

FIGURE 2. (*a*) Streamwise spectra $|u_m|$ averaged in the azimuthal direction; (*b*) azimuthal spectra $|u_n|$ averaged in the streamwise direction at $r = 3.4$ and $t = 1.124\pi$ for $\alpha = 4$ and $R_\delta = 6000$ (—+—, streamwise velocity component; – – × – – radial velocity component; · · · ∗ · · ·, azimuthal velocity component).

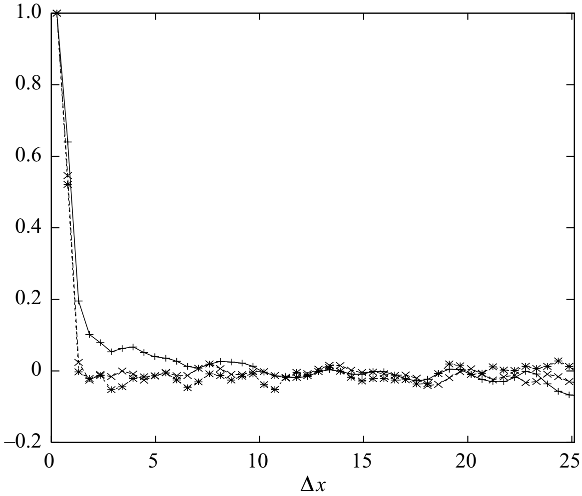

FIGURE 3. Two-point spatial autocorrelation functions in the streamwise direction at $r = 3.4$ and $t = 1.124\pi$ for $\alpha = 4$ and $R_\delta = 6000$ (—+—, R_{uu}; – – × – –, R_{vv}; · · · ∗ · · ·, R_{ww}).

To check that the limited size of the computational box does not significantly affect the dynamics of the observed vortex structures, the instantaneous two-point spatial autocorrelation function R_{uu} for the velocity field has been computed. R_{uu} is defined by

$$R_{uu} = \frac{\overline{u(x, r, \theta, t)u(x + \Delta x, r, \theta, t)}}{\overline{u(x, r, \theta, t)u(x, r, \theta, t)}}, \tag{2.17}$$

where u is the generic velocity component and an overbar denotes the average along the x- and θ-directions. Figure 3 shows the autocorrelation functions evaluated at $r = 3.4$ and at the phase of the cycle when turbulence starts to appear; similar results are obtained when different distances from the wall or different phases of the cycle are considered, if turbulence is present. The instantaneous autocorrelation functions are almost zero at half the computational domain and, hence, the numerical predictions can be used to investigate the turbulence structure and to isolate the basic process generating turbulence. Moreover, some of the runs have been repeated with larger values of L_x^*. In particular for $R_\delta = 6000$, $\alpha = 4$, $U_s^*/\hat{U}_o^* = 0$, results have been obtained with $L_x^* = 100.48\delta^*$ such that the length of the computational box is roughly 7000 wall units. For the large computational box, the number of grid points has been doubled in the streamwise direction and $193 \times 49 \times 129$ grid points have been used in the streamwise, radial and azimuthal directions respectively; no significant difference with respect to the results obtained with the smaller computational box has been found.

3. Numerical results

First, the code described above has been used to identify the conditions which trigger the transition from the laminar to the turbulent regime, when the flow in the pipe is purely oscillatory, i.e. when G_s^*/G_o^* is set equal to zero. Attention is focused on values of the parameters which are relevant for the investigation of the flow behaviour in the human circulatory and respiratory systems. As described in Pedley (1980), the Womersley parameter α ranges from values around 10 in the ascending aorta through values of a few units for the carotid artery down to much smaller values ($O(10^{-3})$) for arterioles and capillaries. Also the Reynolds number R_δ decreases on moving from large arteries to small capillaries from values of a few thousand down to values of order one. Similar values characterize the respiratory system (see Bedoya *et al.* 2003).

As already pointed out, wall imperfections as specified by (2.2) are introduced to trigger transition to turbulence. For the plane wall case, Vittori & Verzicco (1998) used two harmonic components of small amplitude ($N = 2$ in (2.2)): the first component was periodic in the streamwise direction with a wavelength equal to $12.57\delta^*$ and the second one was periodic in the azimuthal direction with a wavelength equal to $6.28\delta^*$. The wavelength of the first component was chosen on the basis of the linear stability analysis of Blondeaux & Seminara (1979) who showed that, in the plane wall case, the most unstable mode is two-dimensional and has a wavelength equal to $12.57\delta^*$. The second component was chosen with the same spanwise spatial periodicity as that of the three-dimensional perturbations which Akhavan *et al.* (1991*b*) showed to have the maximum growth rate when interacting with a pre-existing finite-amplitude two-dimensional wave. In the present case, we follow Vittori & Verzicco (1998) and start the numerical simulations by fixing N equal to 2, $a_1 = 1$, $\alpha_1 = 0.5$, $\gamma_1 = 0$, $\phi_1 = 0$, $a_2 = 0.1$, $\alpha_2 = 0$, $\gamma_2 = n_\alpha$, $\phi_2 = 0$, n_α being the integer closest to α. As discussed in the following, further runs, with double or half the wavelengths of the wall waviness or with random wall imperfections, show that the process which leads to turbulence is not significantly affected by the wavelength of the wall waviness. Finally, ϵ is set equal to 0.005. However, numerical simulations have also been carried out for different values of ϵ to show how the critical values of the Reynolds number are affected by the amplitude of the wall imperfections.

A first set of runs is made for $\alpha = R^*/\delta^* = 4$ and six different values of the Reynolds number. For the smallest values of R_δ (namely 3000, 4000), the perturbations of the basic flow described by (2.3)–(2.7) remain of order ϵ, i.e. the order of magnitude of the amplitude of the wall waviness, and the flow regime can be assumed laminar. For the largest values of R_δ (namely 5000, 6000, 7000, 8000), the perturbations induced by

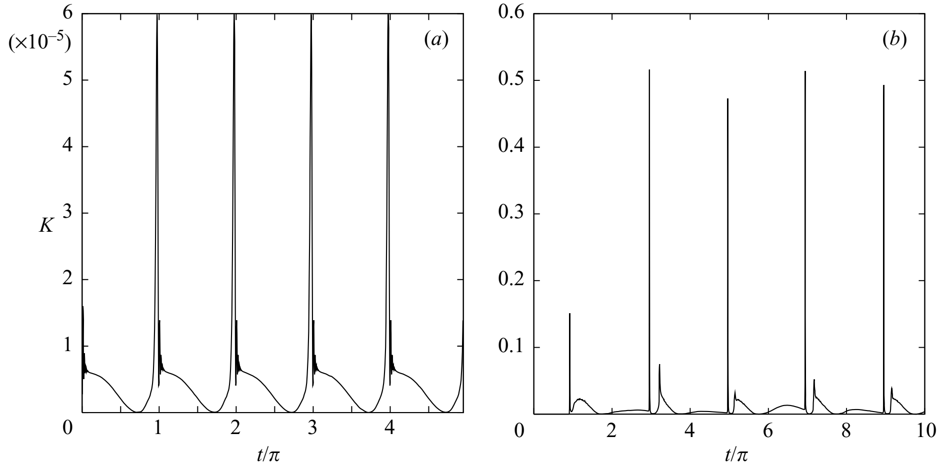

FIGURE 4. Time development of the kinetic energy K of the flow perturbations for $\alpha = 4$ and (*a*) $R_\delta = 4000$, (*b*) $R_\delta = 8000$.

the wall imperfections grow at particular phases of the cycle and attain large values giving rise to turbulence, even though turbulence is not present throughout the whole cycle and for $R_\delta = 5000$ a large number of cycles is necessary to observe turbulence appearance. Hence, the main characteristics of the intermittently turbulent regime, as defined by Vittori & Verzicco (1998), can be recognized. The kinetic energy K of the velocity perturbations of the basic laminar flow, per unit length of the pipe, is plotted versus time in figures 4(*a*) and 4(*b*) for $R_\delta = 4000$ and $R_\delta = 8000$, respectively. K is defined by

$$K = \frac{\pi}{L_x} \int_0^{L_x} \left[\int_0^{\alpha} (u'^2 + v'^2 + w'^2) r dr \right] \mathrm{d}x, \tag{3.1}$$

where (u', v', w') are the perturbations of the velocity field with respect to the laminar value. For $R_\delta = 4000$, after an initial short transient, the kinetic energy $K(t)$ turns out to be periodic with period π. Moreover, K is of order ϵ^2 and the flow perturbations have the spatial structure of the wall waviness (2.2) as shown in figure 5 and figure 6, where the radial and azimuthal velocity components, respectively, are plotted in the cross-section $x = 9.43$ and in the plane $\theta = 1.14\pi$. In figures 5 and 6 the coordinates y and z are introduced such that (x, y, z) is a Cartesian coordinate system.

To show the accuracy of the results and their independence from the numerical grid, in figure 7 the time development of K is shown for the same values of the parameters as in figure 4 but doubling the number of grid points both in the streamwise and azimuthal directions (broken line) and halving the Courant–Friedrich–Levy number (CFL) used in the simulation to fix the value of the time step Δt_{max} (dot-dashed line).

In the following, to give an idea of the major features of the three-dimensional flow field generated by the growth of the flow perturbations induced by the wall waviness, plots of the streamwise component ω_x of the vorticity are shown, since this vorticity component vanishes for axisymmetric flows and significant values of ω_x can be associated with turbulence appearing. When R_δ is equal to 8000 and turbulence appears, K is characterized by much larger values which are no longer related to ϵ. The perturbations induced by the wall imperfections grow because of the flow instability and after a short transient the flow attains a ‘regime’ state. Two different time behaviours of the flow in a half-cycle can be observed. In one case (see figure 4*b*

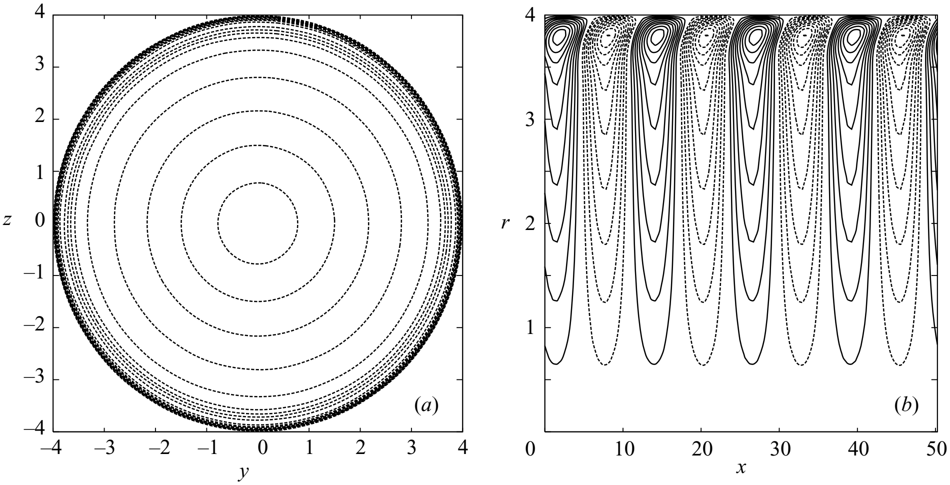

FIGURE 5. Radial velocity component for $\alpha = 4$ and $R_\delta = 4000$ at $t = 1.7\pi$ and (*a*) $x = 9.43$, (*b*) $\theta = 1.14\pi$ (contour interval $\Delta = 2 \times 10^{-6}$; broken lines = negative values; solid lines = positive values).

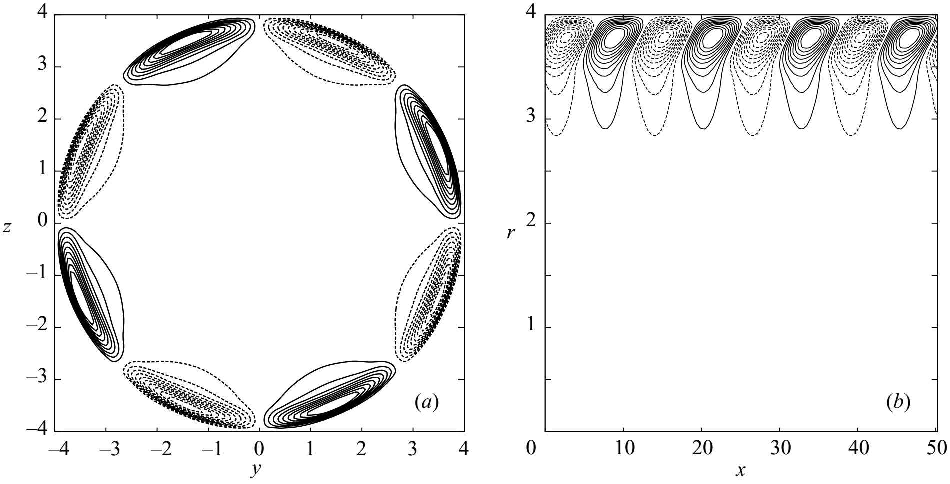

FIGURE 6. Azimuthal velocity component for $\alpha = 4$ and $R_\delta = 4000$ at $t = 1.7\pi$ and (*a*) $x = 9.43$, (*b*) $\theta = 1.14\pi$ (contour interval $\Delta = 4\ 10^{-8}$; broken lines = negative values; solid lines = positive values).

for $2\pi < t < 3\pi$, $4\pi < t < 5\pi$, $6\pi < t < 7\pi, \ldots$), there is a fast growth of K just before flow reversal. Figure 8, which is an enlargement of figure 4(*b*) for $4\pi < t < 6\pi$, shows this typical behaviour of $K(t)$. Figure 9, where the streamwise vorticity component is plotted in the cross-section $x = 35$ and in the plane $\theta = 0.5\pi$ at $t = 4.19\pi$, shows that initially the growth of K is induced by the growth, which takes place close to the wall, of a mode characterized by a wavelength in the azimuthal direction equal to $2\pi/3$ and in the streamwise direction equal to about $12.56\delta^*$. Then, a different mode, which is characterized by azimuthal and streamwise wavelengths equal to 2π and $25.12\delta^*$ respectively, grows quickly giving rise to a coherent structure of the flow different from that displayed in figure 9 (see figures 10 and 11 where the streamwise vorticity

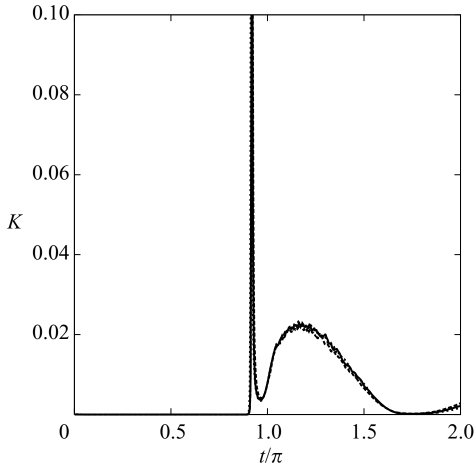

FIGURE 7. Time development of the kinetic energy K of the flow perturbations for $\alpha = 4$, $R_\delta = 8000$ and $\Delta t_{max} = 10^{-4}$. Continuous line, $N_x = 97$, $N_r = 49$, $N_\theta = 129$, $CFL = 1$; broken line, $N_x = 193$, $N_r = 49$, $N_\theta = 257$, $CFL = 1$; dotted-dashed line, $N_x = 97$, $N_r = 49$, $N_\theta = 129$, $CFL = 0.5$.

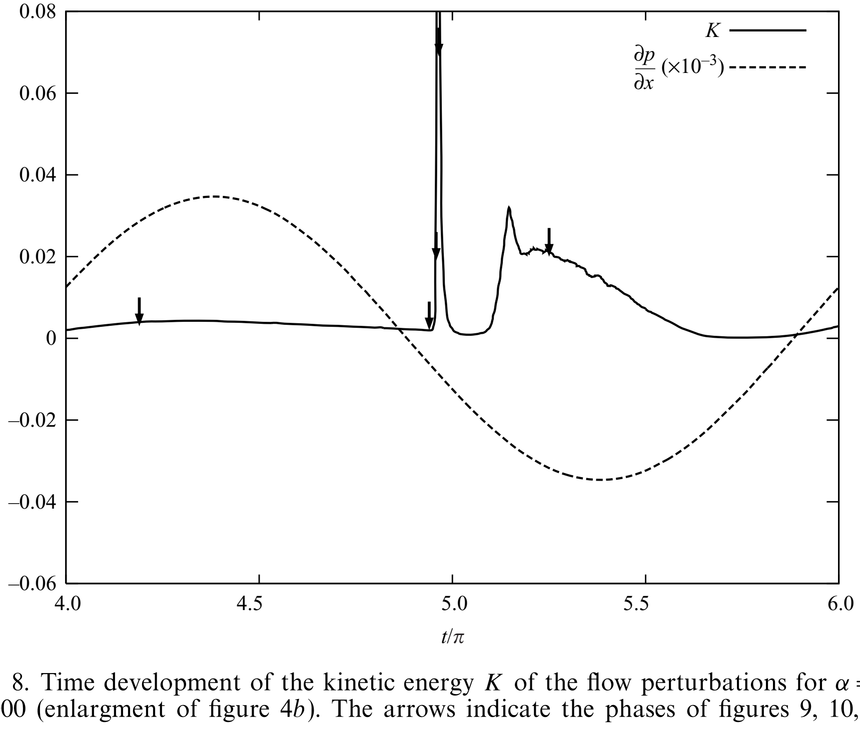

FIGURE 8. Time development of the kinetic energy K of the flow perturbations for $\alpha = 4$ and $R_\delta = 8000$ (enlargment of figure 4*b*). The arrows indicate the phases of figures 9, 10, 11, 12, and 13.

component is plotted for $x = 15$ and $\theta = 0.94\pi$ at $t = 4.94\pi$ and for $x = 19.37$ and $\theta = 1.14\pi$ at $t = 4.598\pi$ respectively). Later, this coherent flow structure breaks down generating small-scale eddies and, hence, turbulence (see figure 12*a* which shows the streamwise vorticity component for $x = 34$ at $t = 4.965\pi$). Because of the generation of small-scale incoherent vortices, large dissipative effects are present which induce a

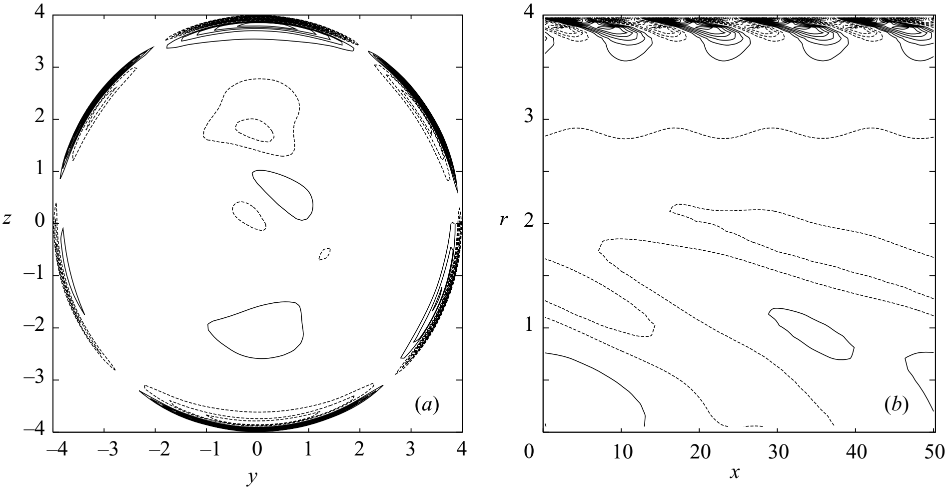

FIGURE 9. Streamwise vorticity component for $\alpha = 4$ and $R_\delta = 8000$ at $t = 4.19\pi$ and (*a*) $x = 35$, (*b*) $\theta = 0.5\pi$ (contour interval $\Delta = 10^{-3}$; broken lines = negative values; solid lines = positive values).

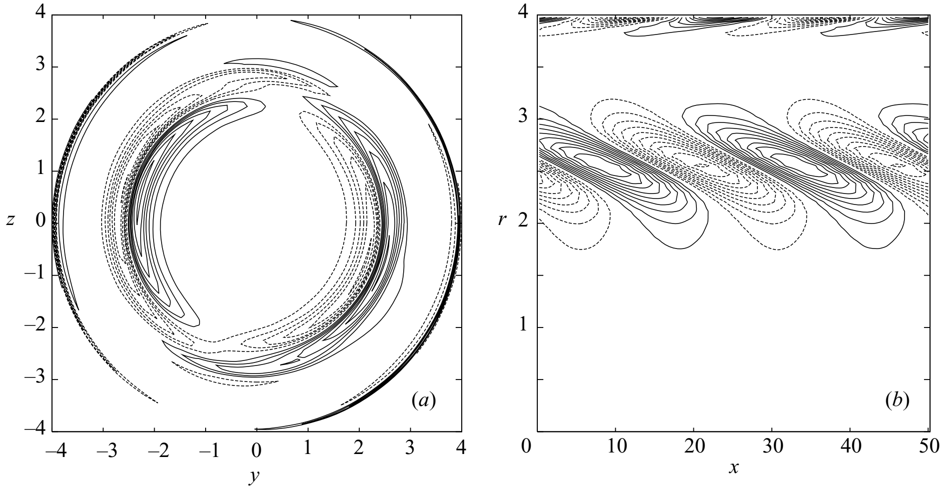

FIGURE 10. Streamwise vorticity component for $\alpha = 4$ and $R_\delta = 8000$ at $t = 4.94\pi$ and (*a*) $x = 15$, (*b*) $\theta = 0.94\pi$ (contour interval $\Delta = 1.5 \times 10^{-2}$; broken lines = negative values; solid lines = positive values).

rapid decay of turbulence. However, turbulence survives to the dissipative phase of the cycle (figure 12*b*) and then it grows again (figure 13) during the following half-cycle and pervades a significant part of the cycle (figure 4*b* for $3\pi < t < 4\pi$, $5\pi < t < 6\pi$, $7\pi < t < 8\pi, \ldots$ and figure 8 for $5\pi < t < 6\pi$). Hence, the basic flow is strongly modified by the Reynolds stresses and the growth of the coherent mode previously observed before flow reversal is not induced. Then, the dissipative phase of the cycle occurs again and the flow relaminarizes. Even though the length of the numerical simulation does not allow any definitive conclusions to be drawn, it appears that the flow attains a ‘regime’ state such that there is an alternation of these two behaviours. Therefore, the symmetry of the flow is broken by the turbulence and a steady drift is generated

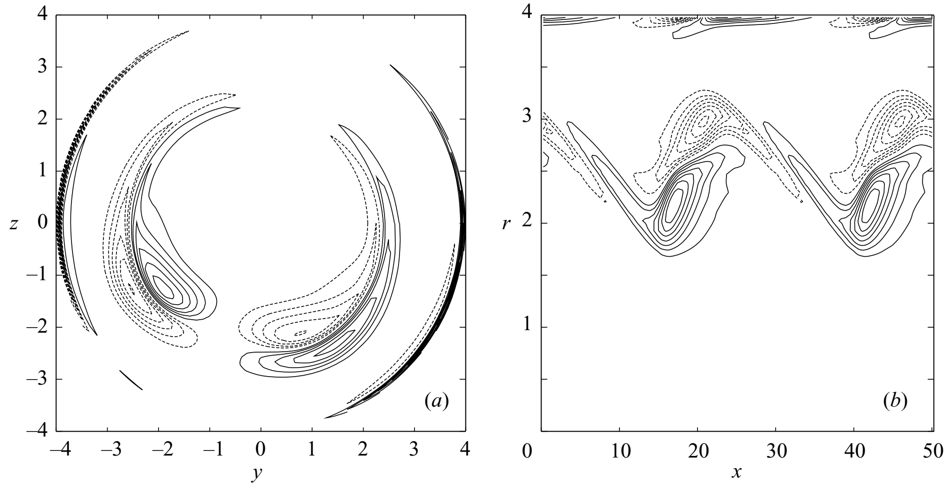

FIGURE 11. Streamwise vorticity component for $\alpha = 4$ and $R_\delta = 8000$ at $t = 4.958\pi$ and (*a*) $x = 19.37$, (*b*) $\theta = 1.14\pi$ (contour interval $\Delta = 0.2$; broken lines = negative values; solid lines = positive values).

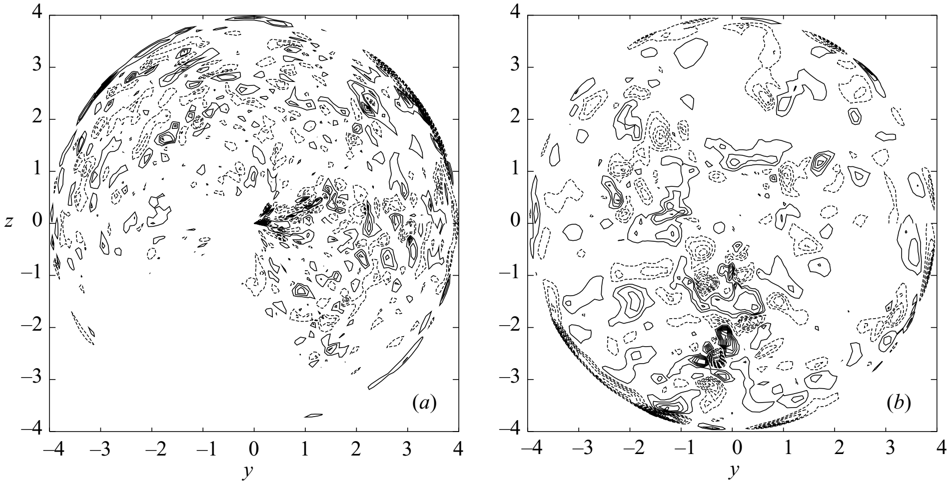

FIGURE 12. Streamwise vorticity component for $\alpha = 4$ and $R_\delta = 8000$: (*a*) $t = 4.965\pi$ and $x = 34$, contour interval $\Delta = 3$; (*b*) $t = 4.98\pi$ and $x = 23$, contour interval $\Delta = 0.3$ (broken lines = negative values; solid lines = positive values).

within the pipe. This phenomenon can be explained on physical grounds by noting that the rapid growth of the mode characterized by a streamwise wavenumber equal to 0.25 and by an azimuthal wavenumber equal to 1, and the subsequent appearance of turbulence, enhances the wall shear stress and leads to a decrease of the peak velocity. During the following half-cycle, because of this decrease of the peak velocity, resonance does not take place and the wall shear stress assumes smaller values, giving rise to large velocities. This phenomenon is clearly shown in figure 14, where the axial velocity is plotted versus time. The instability of the flow with respect to a perturbation different from that forced by wall imperfections can also be observed for different values of the parameters. For example, figure 15 shows the streamwise

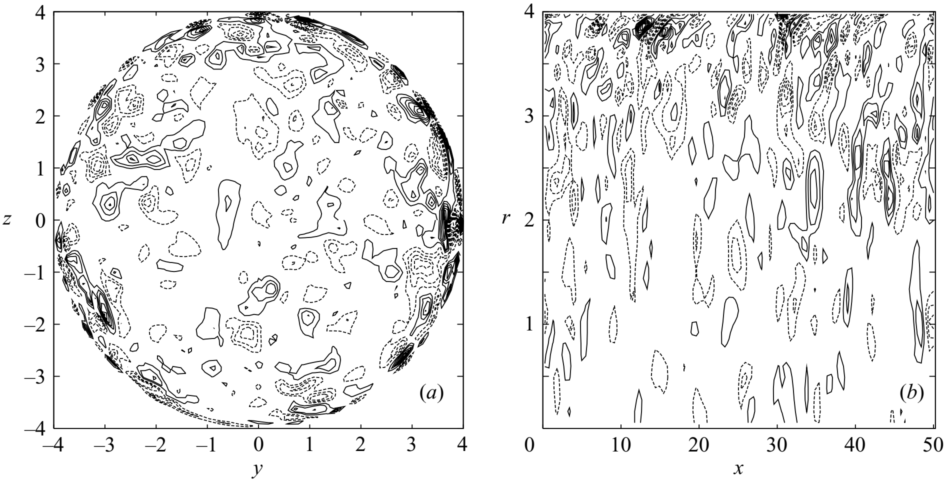

FIGURE 13. Streamwise vorticity component for $\alpha = 4$ and $R_\delta = 8000$ at $t = 5.25\pi$ and (*a*) $x = 20.5$, (*b*) $\theta = 1.84\pi$ (contour interval $\Delta = 0.4$; broken lines = negative values; solid lines = positive values).

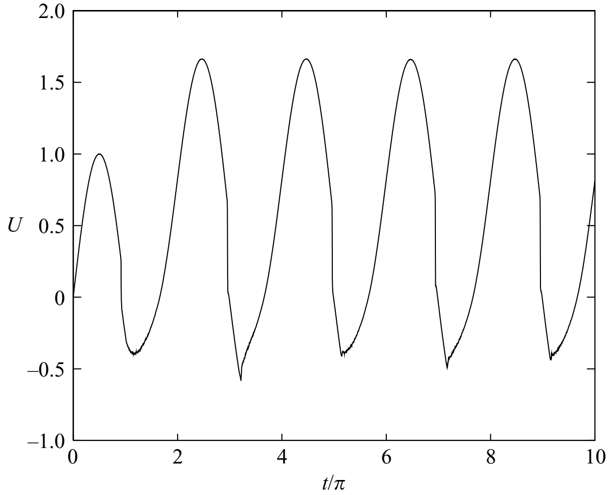

FIGURE 14. Time development of the averaged axial velocity for $\alpha = 4$ and $R_\delta = 8000$ at $r = 0$.

vorticity component plotted in a section of the pipe for $\alpha = 4$ and $R_\delta = 6000$, at two different phases of the cycle. At $t = 0.75\pi$, only the perturbation forced by the wall waviness can be observed but later on, at $t = 1.81\pi$, a mode characterized by $k_m = 0.5$ and $k_n = 1$ appears and rapidly grows.

At this stage, it is appropriate to investigate the sensitivity of the results to the characteristics of the wall imperfections. Let us identify as case (i) the wall waviness used to obtain the numerical results described so far. Two further simulations have been made with $\alpha = 4$ and $R_\delta = 8000$ but halving the wavenumbers α_1, γ_1, α_2, γ_2 (simulation (ii)), and doubling the wavenumbers α_1, γ_1, α_2, γ_2 (simulation (iii)).

In figure 16, the time development of K is plotted for the three different wall imperfections (i, ii, iii) described above, and in figures 17 and 18, the streamwise vorticity component is plotted in a pipe section at the beginning of the rapid growth

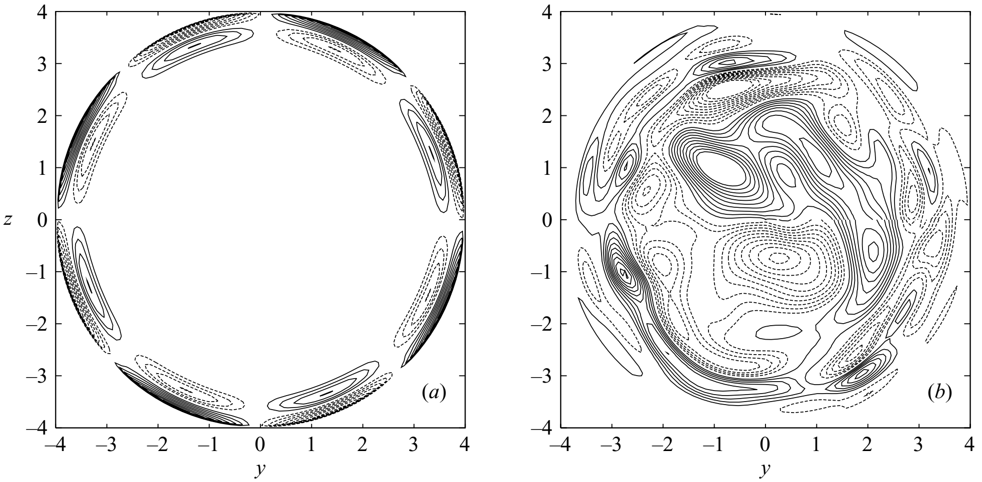

FIGURE 15. Streamwise vorticity component for $\alpha = 4$ and $R_\delta = 6000$ and (*a*) $x = 2.7$, $t = 0.75\pi$ (contour interval $\Delta = 4 \times 10^{-5}$), (*b*) $x = 22$, $t = 1.81\pi$ (contour interval $\Delta = 4 \times 10^{-3}$); broken lines = negative values; solid lines = positive values.

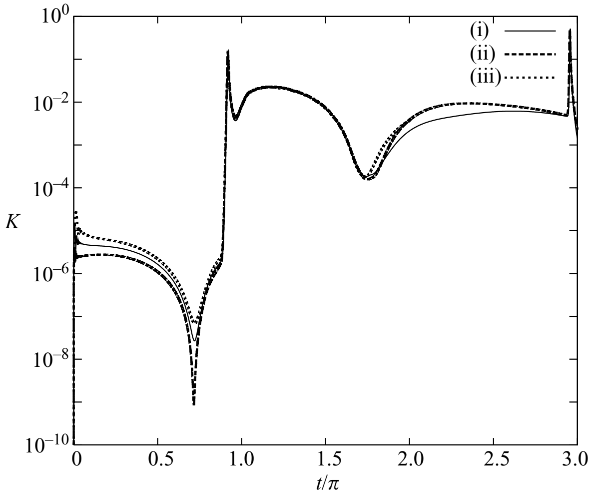

FIGURE 16. Time develpoment of the kinetic energy K of the flow perturbations for $\alpha = 4$, $R_\delta = 8000$ and the three wall wavinesses defined as (i), (ii), (iii) in the text.

of K and just after its rapid decay. The results obtained show that the characteristics of the wall imperfections have no significant influence on the transition process and on turbulence structure if the Reynolds number is well above its critical value. At the beginning of the simulations the flow perturbations have the spatial structure forced by the wall waviness but then, in all cases, the mode characterized by a streamwise wavenumber equal to 0.25 and by an azimuthal wavenumber equal to 1 grows (figure 17) and eventually turbulence appears (figure 18).

A further simulation has been made for $\alpha = 4$, $R_\delta = 8000$ and introducing $N = 25$ harmonic components in (2.2) characterized by random values of a_n, φ_n but such that the final amplitude of the wall waviness is equal to that of the previous numerical experiments; α_n ranges from $8\pi/L_x$ to $16\pi/L_x$ and γ_n ranges from 8π to 16π. Figure 19

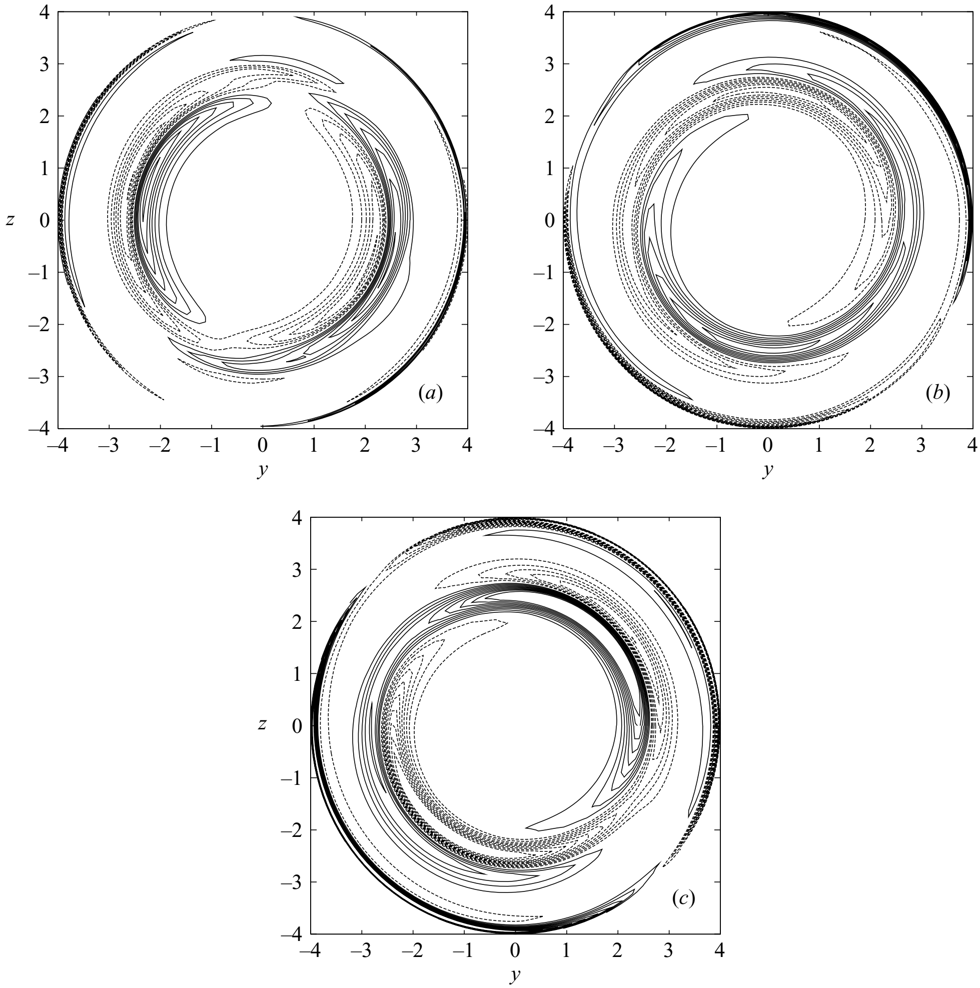

FIGURE 17. Streamwise vorticity component for the three wall wavinesses (i), (ii), (iii). $\alpha = 4$, $R_\delta = 8000$ and $x = 14.6$: (*a*) waviness (i), $t = 4.94\pi$, contour interval $\Delta = 1.5 \times 10^{-2}$, (*b*) waviness (ii), $t = 0.87\pi$, $\Delta = 10^{-3}$, (*c*) waviness (iii), $t = 0.87\pi$, $\Delta = 10^{-3}$; broken lines = negative values; solid lines = positive values.

shows the wall geometry η as a function of x and θ. The time development of K for the random wall imperfection is shown in figure 20 and the streamwise vorticity component in a section of the pipe just before the rapid growth of K and at the end of its decay is shown in figure 21. The results obtained show that even a random pipe wall waviness does not induce any qualitative difference in the transition process. Hence, it can be concluded that wall imperfections are necessary to trigger turbulence but the geometry of the wall waviness has no influence on the turbulence structure.

On the other hand, the results of Vittori & Verzicco (1998) show that the transition process in a flat Stokes boundary layer is affected by the amplitude of the wall imperfections. Hence, it is worth investigating how the value of ϵ affects the present results. In figure 22, $\overline{K}$, the time-averaged value of K ($\overline{K} = \int_0^{2\pi} K\,\mathrm{d}t/(2\pi)$) is plotted versus R_δ for $\alpha = 4$, choosing the wall waviness (i) and three different values of ϵ (0.0025, 0.005, 0.008). The laminar as well as the intermittently turbulent regimes,

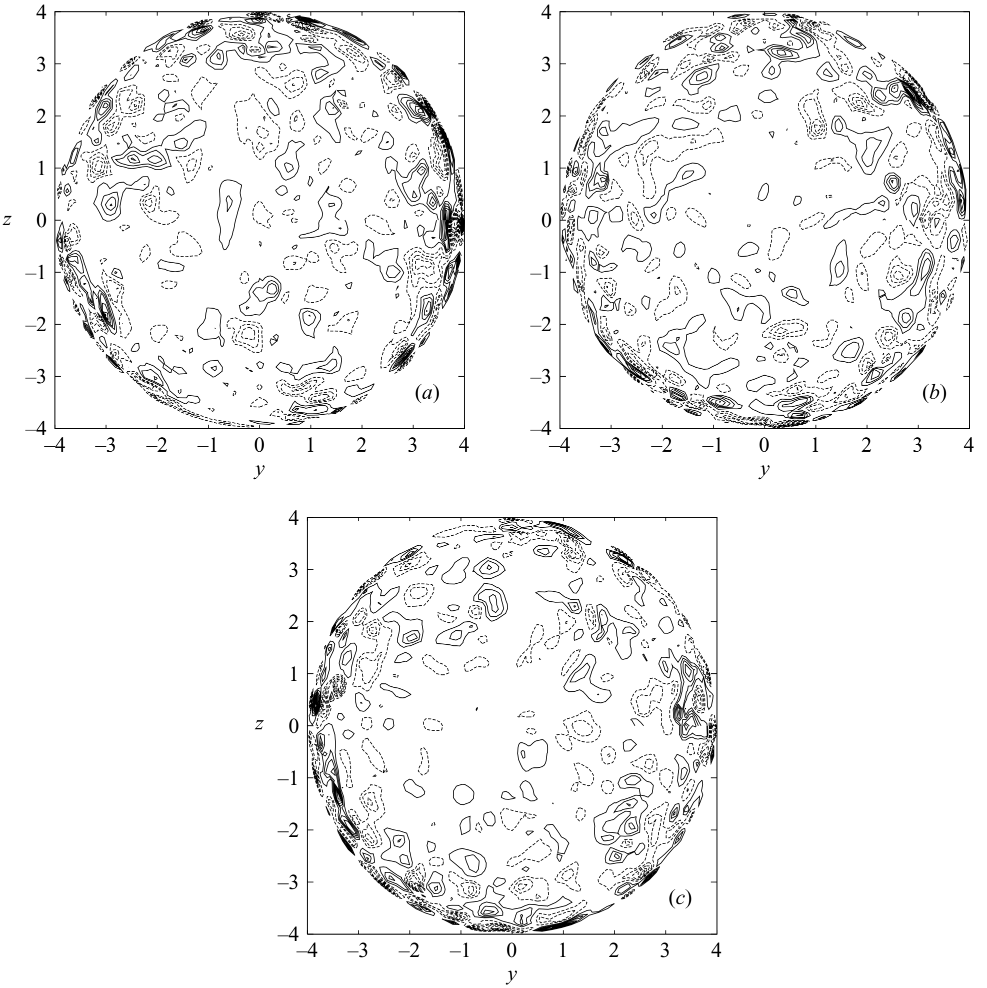

FIGURE 18. Streamwise vorticity component for the three wall wavinesses (i), (ii), (iii). $\alpha = 4$ and $R_\delta = 8000$ and $x = 20.5$ (contour interval $\Delta = 0.4$): (*a*) waviness (i), $t = 5.25\pi$, (*b*) waviness (ii), $t = 1.12\pi$, (*c*) waviness (iii), $t = 1.12\pi$; broken lines = negative values; solid lines = positive values.

defined in the introduction and named regimes (*a*) and (*c*) can be identified. In the laminar regime, which can be observed for R_δ smaller than 4000, $\overline{K}$ is practically independent of R_δ and is proportional to ϵ^2. In the intermittently turbulent regime (R_δ larger than 5000), $\overline{K}$ is weakly dependent on R_δ and is almost independent of ϵ. In order to observe the disturbed regime, which takes place for R_δ falling in the range 4000–5000 and is characterized by values of $\overline{K}$ which depend on both R_δ and ϵ, it would be necessary to make further long runs, which are too expensive from the computational point of view.

By comparing the results obtained so far with those obtained by Vittori & Verzicco (1998), it appears that the oscillatory flow in a pipe of relatively small radius is much more stable than the oscillatory flow over a flat wall, where the presence of turbulence is detected when R_δ is larger than a value close to 550. Further simulations show that the stabilizing effect decreases on increasing the radius of the pipe, i.e. on increasing

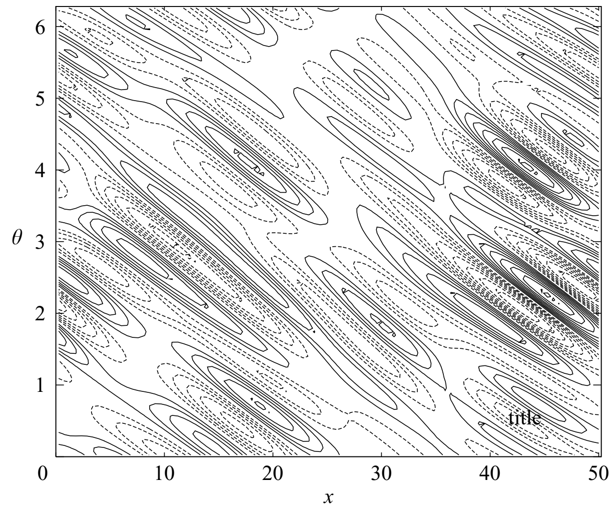

Figure 19. The geometry of the pipe wall when a random imperfection is present (contour interval $\Delta = 1.5 \times 10^{-4}$).

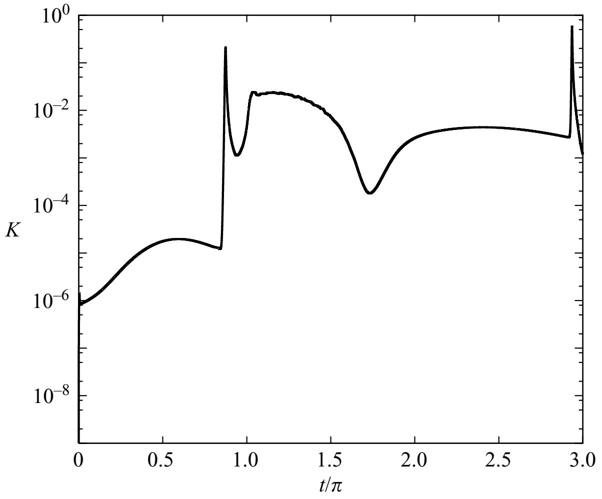

Figure 20. Time development of K for $\alpha = 4$ and $R_\delta = 8000$ when a random wall imperfection is present.

the value of α (see, for example, figure 23). When α is equal to 4, the values of K are of order ϵ^2 and an analysis of the velocity field shows that the flow regime is laminar; when α is equal to 6, turbulence starts to appear intermittently. However, it is reasonable to expect that curvature effects become negligible and the results of the flat wall case are recovered for values of α larger than a threshold value. In figure 24 the laminar and turbulent cases are shown in the $R_\delta - \alpha$ plane and the results indicate that this threshold value of α is around 10. In the same figure, the critical values of the Reynolds number measured by Hino *et al.* (1976), Tromans (1976) and Lodhal *et al.* (1998) are also shown. The experimental values of the critical Reynolds number are smaller than the numerical ones because, as previously pointed out, the transition

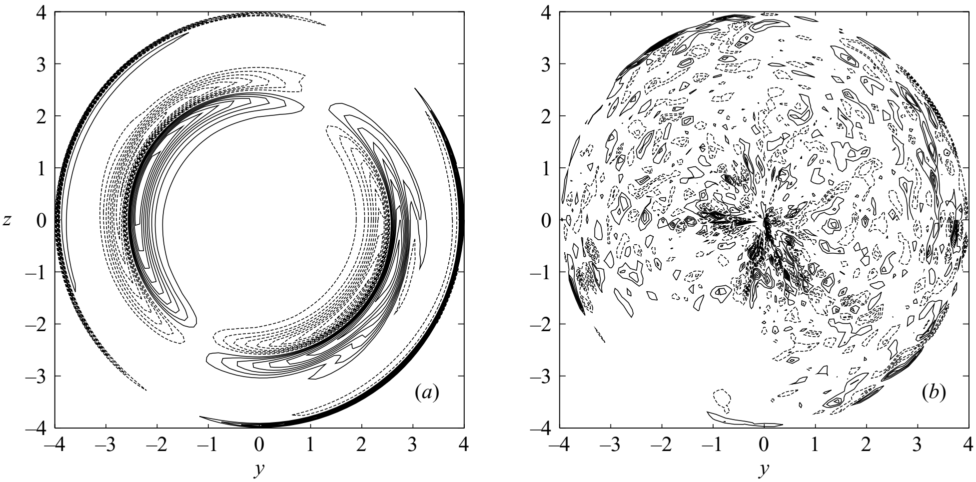

FIGURE 21. Streamwise vorticity component for the geometry of the pipe wall when a random imperfection is present for $\alpha = 4$ and $R_\delta = 8000$: (*a*) $x = 45$ $t = 2.923\pi$ (contour interval $\Delta = 0.01$), (*b*) $x = 5.8$ $t = 2.94\pi$, contour interval $\Delta = 2.5$; broken lines = negative values; solid lines = positive values.

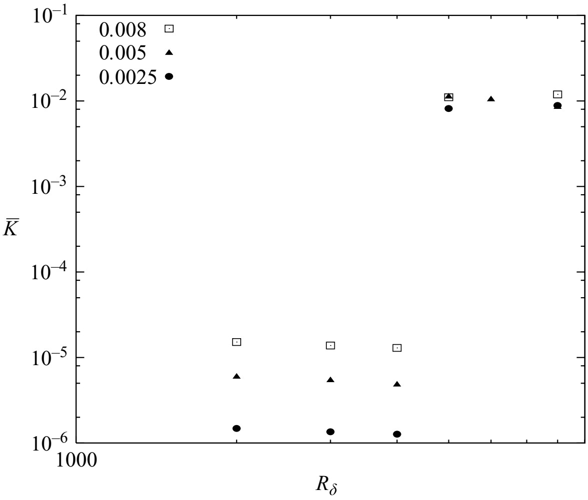

FIGURE 22. Time-averaged kinetic energy $\overline{K}$ of the flow perturbations versus the Reynolds number R_δ for $\alpha = 4$ and different values of ϵ.

process is largely influenced by the level of the perturbations, which is very small in the numerical simulations.

Both experimental and numerical investigations provide a lot of information on turbulence structure in steady pipe flows at high Reynolds numbers. However, much less is known about unsteady flows. Hence, it is of interest to investigate turbulence dynamics in the present case. Figure 25(*a*) shows the production P, the dissipation D and the redistribution R, appearing in the equation for the turbulent kinetic energy, plotted versus the coordinate $y^+ = (R^* - r^*)u^*_\tau/\nu^*$ at a particular phase ($t = 5.25\pi$) of the cycle, when turbulence is present, for $\alpha = 4$ and $R_\delta = 8000$. In figure 25, the profiles of the various contributions to the turbulence budget are normalized using the viscous

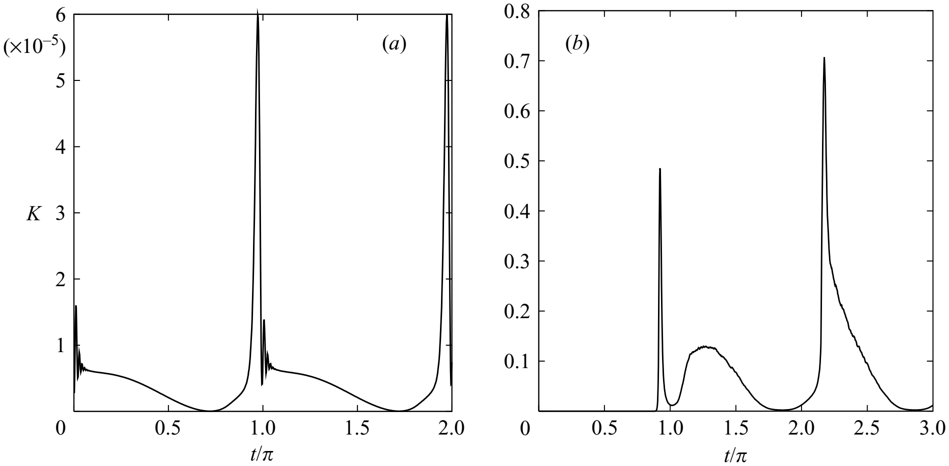

FIGURE 23. Time development of the kinetic energy K of the flow perturbations for $R_\delta = 4000$ and (a) $\alpha = 4$, (b) $\alpha = 6$.

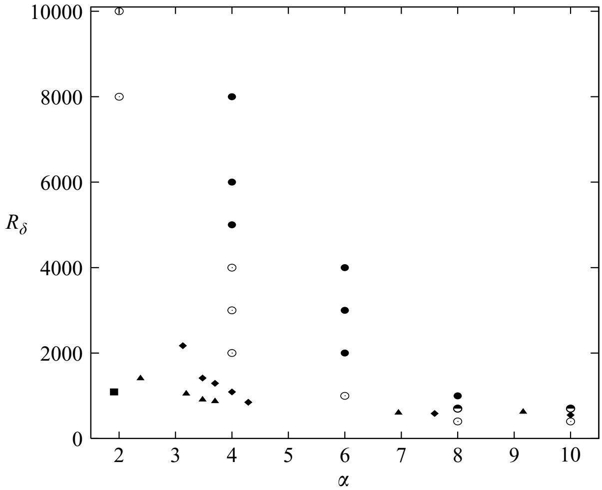

FIGURE 24. Laminar (open circles), disturbed laminar (half-filled circles) and intermittently turbulent (filled circles) cases in the plane α–R_δ according to the numerical simulations. Experimental transition limits between laminar and turbulent cases: filled squares Hino *et al.* (1976); filled triangles Tromans (1976); filled diamonds Lodhal *et al.* (1998).

scales ν^*/u^*_τ, u^*_τ, ν^*/u^{*2}_τ for the length, the velocity and the time, respectively (u^*_τ is the instantaneous shear velocity). By comparing the results plotted in figure 25(a) with those available for steady pipe flows (see, for example, Pope 2000, p. 285), it appears that the turbulence dynamics is similar and the different contributions to the turbulent budget have the same order of magnitude. The production term increases from zero at the wall and it reaches its peak value well within the buffer layer. Around this peak, production exceeds dissipation and the excess energy produced is transported away. An analysis of the different contributions to the redistribution term shows that the pressure transport is small while turbulent convection transports energy both toward the wall and into the expected log-law region. Viscous transport moves kinetic energy

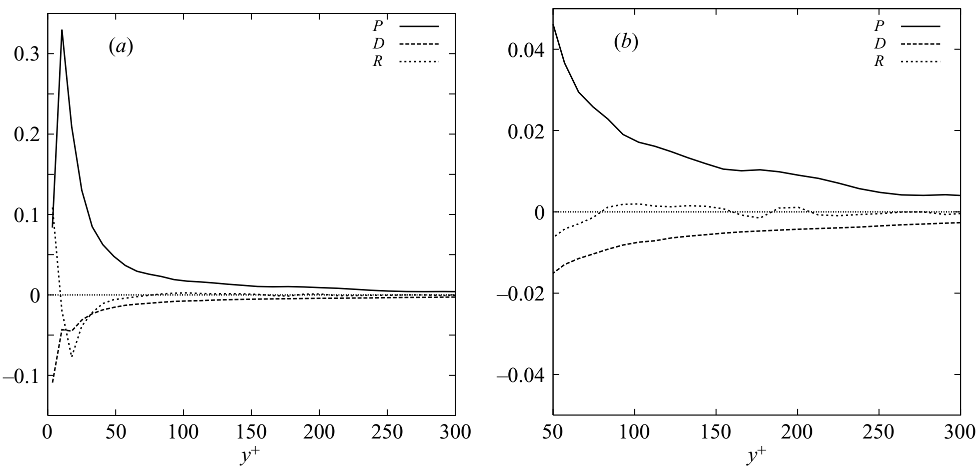

FIGURE 25. (*a*) Different terms of the turbulent-kinetic-energy budget for $\alpha = 4$ and $R_\delta = 8000$ at $t = 5.25\pi$; (*b*) enlargement of (*a*) for $y^+ > 50$.

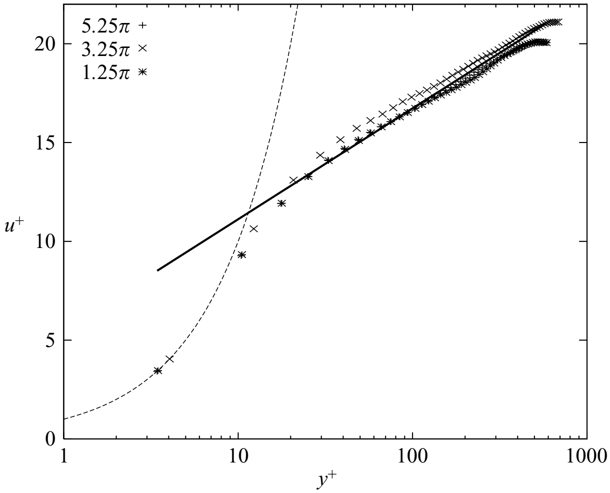

FIGURE 26. Mean velocity profiles, using wall units, at different phases of the cycle, for $\alpha = 4$ and $R_\delta = 8000$ (solid line = logarithmic law; broken line = linear velocity in the viscous sublayer).

all the way to the wall. The peak dissipation occurs at the wall, where the kinetic energy of turbulence vanishes. Although the fluctuating velocity practically vanishes at $r = \alpha$, the fluctuating strain rate and dissipation do not. The dissipation at the wall is balanced by the redistribution term and in particular by viscous transport, the other terms being zero.

Moving away from the wall the redistribution term tends to zero more rapidly than P and D, which balance each other (see figure 25*b*). Therefore, an equilibrium layer can be identified. On the basis of this finding, it can be argued that a logarithmic velocity profile is present and, by plotting the value of u averaged along the θ- and x-directions as function of r in the semi-logarithmic plane $(\ln y^+, u^+)$ at different phases of the cycle but all characterized by turbulence presence, it can be seen that a log-law behaviour can be identified for $y^+ > 50$ (see figure 26). Moreover, an estimate

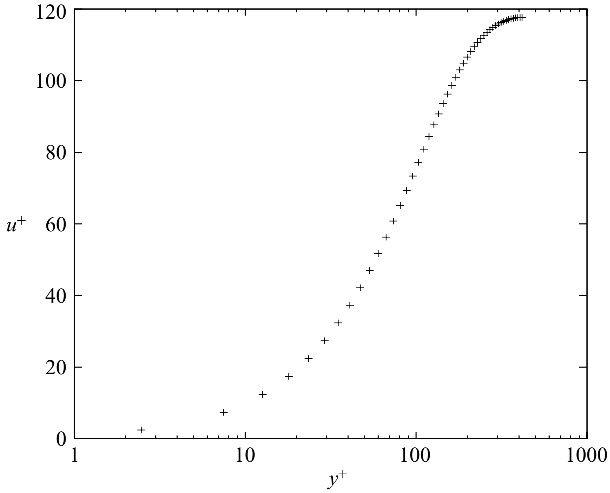

FIGURE 27. Mean velocity profiles, using wall units, at $t = 4.315\pi$ for $\alpha = 4$ and $R_\delta = 8000$.

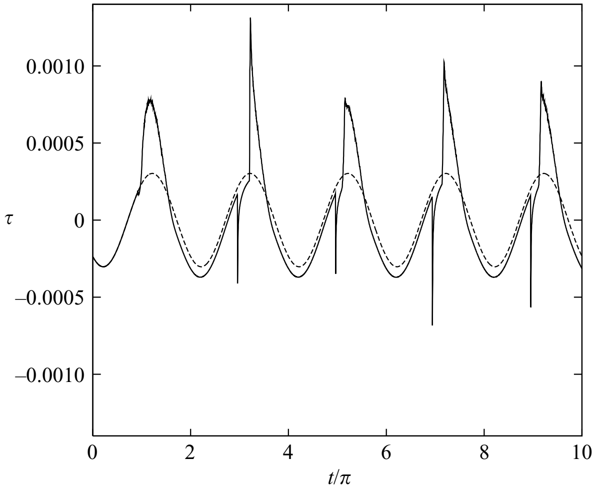

FIGURE 28. Time development of the wall shear stress τ for $\alpha = 4$ and $R_\delta = 8000$.

of the slope of the straight line interpolating the numerical results leads to a value of the von Kármán constant equal to 0.4 ± 10 %, in agreement with that found in the literature for steady flows, and to a slightly time-dependent value of the constant which provides u^+ for $\ln y^+ = 0$ but always close to 5.5 (5.5 ± 15 %). A rough estimate of $\partial K/\partial t$ based on the results of figure 25 suggests that, at $t = 5.25\pi$, K is growing and an enlargement of figure 8 around $t = 5.25\pi$ shows that $\partial K/\partial t$ is instantaneously positive. Even though unsteady effects play a minor role in the turbulence dynamics during those parts of the cycle characterized by turbulence presence, they are quite important during the other parts and the velocity profile does not display a log-law in the phases of the cycle characterized by large negative values of the axial velocity (see figure 27).

The time development of the wall shear stress τ is plotted in figure 28. The rapid growth of the coherent vortex structures shown in figures 10 and 11 leads to changes

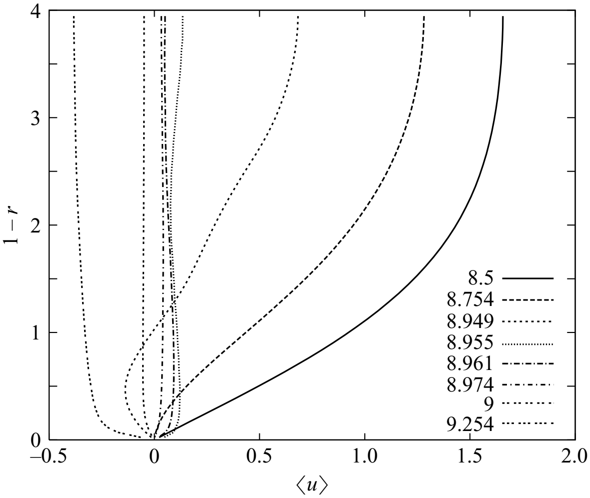

FIGURE 29. Mean velocity profiles for $\alpha = 4$ and $R_\delta = 8000$ at different phases of the cycle around $t = 8.95\pi$.

of the mean velocity profile and to sharp negative peaks of the wall shear stress. The mean velocity profiles just before $t = 8.95\pi$, when a negative peak of the wall shear stress can be observed, show that the mean flow is decelerating and in particular at $t = 8.949\pi$ the velocity close to the wall is already negative inducing a positive wall shear stress, even though far from the wall the velocity is still positive (figure 29). At this stage the appearance of the three-dimensional coherent vortex structures, shown for example in figures 10 and 11, induces a strong mixing and a momentum transfer, with fluid characterized by positive axial velocity moving close to the wall. This causes the sudden change of the wall shear stress, which assumes large negative values. However, because of the pressure gradient, the mean flow keeps decelerating and later on the fluid velocity becomes negative in the whole pipe section, inducing a positive wall shear stress. Moreover, figure 28 shows that, when turbulence appears, the wall shear stress is greatly enhanced by turbulent eddies, whereas the laminar value is recovered when turbulence is damped. The small differences in τ with respect to the theoretical laminar value, during the phases of the cycle characterized by the absence of turbulence, are due to the delaying effects that turbulence has on the mean flow rate. Similar results are obtained for other values of α and R_δ for which turbulence is triggered.

An investigation of the effects of the steady component of the pressure gradient on the stability of the flow has been carried by performing some simulations for $\alpha = 4$. An analysis of the results shows that the steady velocity component has a destabilizing effect. For $R_\delta = 4000$ and $U_s/U_o = 0$, the oscillatory flow in the pipe turns out to be stable. When U_s/U_o is increased, for small values of U_s/U_o the flow remains laminar but as soon as U_s/U_o becomes larger than a value between 0.5 and 1, the laminar flow is destabilized and turbulence appears close to flow reversal. Examples of the results are shown in figure 30, where K is plotted versus t for $\alpha = 4$, $R_\delta = 4000$ and $U_s/U_o = 0.25, 0.5, 1.0, 2.0$. As already pointed out, for $U_s/U_o = 0.25$ and 0.5, K is of order ϵ^2 but periodic with period 2π because of the presence of the steady component of the pressure gradient. At the beginning of the simulations, the difference between $K(t)$ and $K(t + \pi)$ is small but then it increases because of the rapid growth of the

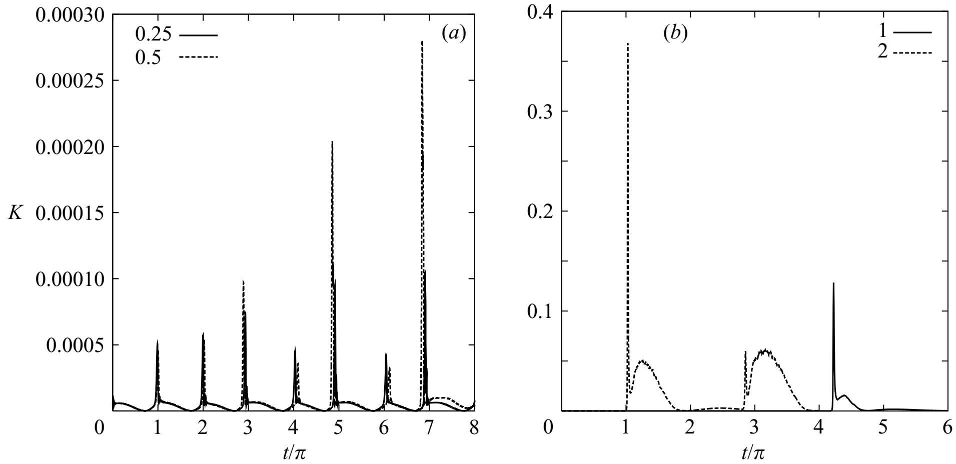

FIGURE 30. Time development of the kinetic energy K of the flow perturbations for $\alpha=4$ and $R_\delta=4000$: (*a*) $U_s/U_o=0.25, 0.5$; (*b*) $U_s/U_o=1, 2$.

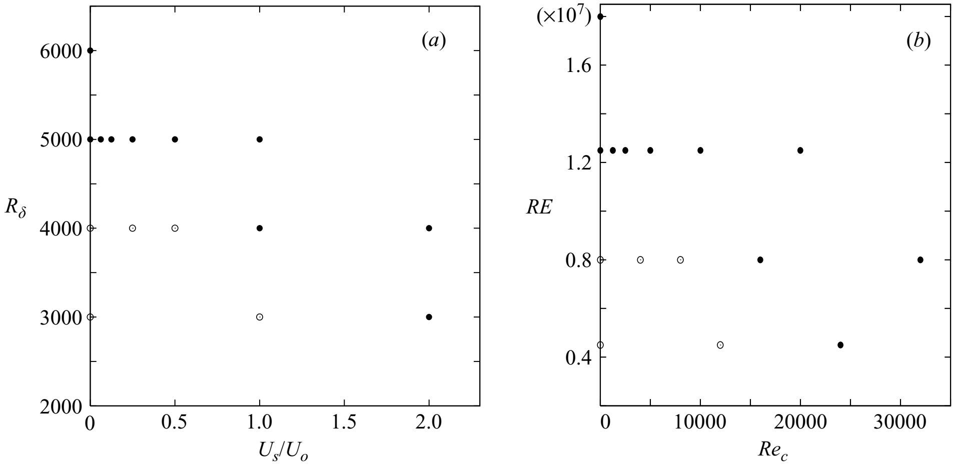

FIGURE 31. Laminar (open circles), disturbed laminar (half-filled circles) and intermittently turbulent (filled circles) cases for $\alpha=4$.

perturbations, which takes place close to flow reversal. A further increase of U_s/U_o leads to turbulence which appears earlier as U_s/U_o is increased (compare $U_s/U_o=1$ and $U_s/U_o=2$).

Of course, larger values of U_s/U_o are required to force transition if smaller values of R_δ are considered. Figure 31(*a*) shows the laminar and the turbulent simulated cases in the U_s/U_o–R_δ plane, while figure 31(*b*) shows the same results in the plane $U_s^* R^*/\nu^*$-RE which was used by Lodhal *et al.* (1998). Comparing the results of figure 31(*b*) with the experimental data by Lodhal *et al.* (1998), it appears that the numerical results qualitatively agree with the laboratory data which show that the presence of a steady velocity component causes a decrease of the critical value of the Reynolds number. Moreover, this decrease becomes larger as U_s/U_o is increased. However, quantitative differences are present which might be induced by the different level of flow perturbations present in the experimental apparatus and those introduced

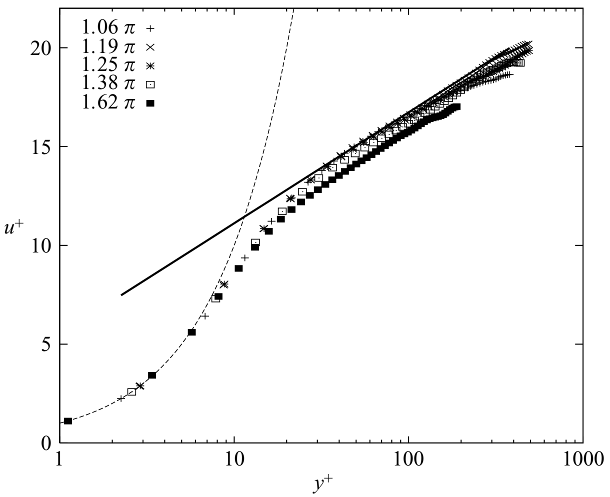

FIGURE 32. Mean velocity profiles, using wall units, at different phases, for $\alpha = 4$, $R_\delta = 5000$ and $U_s/U_o = 1$(solid line = logarithmic law; broken line = linear velocity in the viscous sublayer).

in the numerical simulations by the wall imperfections. Indeed, as already discussed, the value of ϵ significantly affects the transition process.

As in the oscillating case, the dynamics of turbulence in the pulsating case is the same as observed in a steady pipe flow. Figure 32 shows the mean velocity profiles in the semi-logarithmic plane ($\ln y^+, u^+$) at different phases of the cycle for $R_\delta = 5000$, $\alpha = 4$ and $U_s/U_o = 1$, when turbulence is present. In particular, as in the steady case, a log-law behaviour of u^+ can be identified for y^+ larger than 50, an indicator that far from the wall, production and dissipation of turbulence balance each other and the redistribution term is negligible. Moreover, it appears that the value of the von Kármán constant in the pulsating case is equal to that found in the oscillating case and the log-law crosses the ordinate at 5.5.

4. Conclusions

The present numerical simulations allow identification of the critical conditions, i.e. the conditions which lead to turbulence, for the pulsating flow in a pipe of circular cross-section with small imperfections. When U_s/U_o vanishes, i.e. in the oscillatory case, the critical value of the Reynolds number R_δ depends on the Womersley parameter α. For values of α larger than about 10, the critical conditions are similar to those found in the flat wall case by Vittori & Verzicco (1998) and Costamagna *et al.* (2003), but the critical value of the Reynolds number increases as α is decreased. As in the flat wall case, the amplitude ϵ of the wall imperfections does not affect turbulence characteristics in the intermittently turbulent regime, though it might affect flow characteristics in the disturbed laminar regime but this has not been investigated because of computational costs.

As already pointed out in the discussion of the results, close to the marginal conditions the appearance of the turbulence breaks the symmetry of the flow and gives rise to a steady velocity component within the pipe even in the oscillatory case. As shown in figure 4(*b*), turbulence is triggered only where the axial velocity attains its maximum negative values. Of course, this result depends on the initial conditions and different conditions may lead to turbulence when the axial velocity attains its maximum positive values.

The presence of a steady velocity component has a destabilizing effect and induces a decrease of the critical Reynolds number. In any case, the critical values of the Reynolds number seem to be larger than those observed in physiological flows. In the pulsating case, turbulence tends to appear when flow deceleration is stronger, i.e. after the maximum value of the axial velocity is attained. Even though further numerical runs are necessary to fully understand turbulence structures in unsteady flows, the present results indicate that the turbulence dynamics is similar to that observed in steady pipe flows.

The authors are grateful to Professor Paolo Orlandi who provided a first version of the numerical code. R. T. would also like to thank Professor Orlandi for fruitful discussions on the results and for some advice in the further development of the numerical code. Thanks are also due to one of the referees for useful suggestions.

REFERENCES

Akhavan, R., Kamm, R. D. & Shapiro, A. H. 1991*a* An investigation of transition to turbulence in bounded oscillatory Stokes flows. Part 1. Experiments. *J. Fluid Mech.* **225**, 395–422.

Akhavan, R., Kamm, R. D. & Shapiro, A. H. 1991*b* An investigation of transition to turbulence in bounded oscillatory Stokes flows. Part 2. Numerical simulations. *J. Fluid Mech.* **225**, 423–444.

Beam, R. M. & Warming, R. F. 1976 An implicit finite-difference algorithm for hyperbolic system in conservation-law form. *J. Comput. Phys.* **22**, 87–110.

Bedoya, J., Choksi, T., Guo, H. & Pita, A. 2003 Biofluid dynamics of the human respiratory system. In *Congress on Biofluid Dynamics of Human Body Systems*, *Biomedical Engineering, FIU, Miami, FL* D-1 (ed. M. R. Goyal), p. 20.

Blennerhassett, P. J. & Bassom, A. P. 2002 The linear stability of flat Stokes layers. *J. Fluid Mech.* **464**, 393–410.

Blennerhassett, P. J. & Bassom, A. P. 2006 The linear stability of high-frequency oscillatory flow in a channel. *J. Fluid Mech.* **556**, 1–25.

Blondeaux, P. & Seminara, G. 1979 Transizione incipiente al fondo di un'onda di gravitá. *Rendiconti Accad. Naz. Lincei* 67, 407–417.

Blondeaux, P. & Vittori, G. 1994 Wall imperfections as a triggering mechanism for Stokes-layer transition. *J. Fluid Mech.* **264**, 107–135.

Costamagna, P., Vittori, G. & Blondeaux, P. 2003 Coherent structures in oscillatory boundary layers. *J. Fluid Mech.* **474**, 1–33.

Eckmann, D. & Grotberg, J. B. 1991 Experiments on transition to turbulence in oscillatory pipe flow. *J. Fluid Mech.* **222**, 329–350.

Gilbrech, D. A. & Combs, G. O. 1963 *Developments in Theoretical and Applied Mechanics*, vol. 1, p. 292. Plenum.

Goldschmied, F. R. 1970 On the frequency response of viscous compressible fluids as a function of the Stokes number. *Trans. ASME* D: *J. Basic Engng* **92**, 333–347.

Hall, P. 1978 The linear stability of flat Stokes layers. *Proc. R. Soc. Lond.* A **359**, 151–166.

Hino, M., Sawamoto, M. & Takasu, S. 1976 Experiments on transition to turbulence in an oscillatory pipe flow. *J. Fluid Mech.* **75**, 193–207.

Hirschberg, A., J. Gilbert, R. M. & Wijnands, A. P. J. 1996 Shock waves in trombones. *J. Acoust. Soc. Am.* **99**, 1754–1758.

Jimenez, J. & Moin, P. 1991 The minimal flow unit in near-wall turbulence. *J. Fluid Mech.* **225**, 213–240.

Kim, J. & Moin, P. 1985 Application of a fractional-step method to incompressible Navier-Stokes equations. *J. Comput. Phys.* **59**, 308.

Leon, D. F. & Shaver, J. A. 1974 Physiologic principles of heart sounds and murmurus. *American Heart Association Monograph* 46.

LODHAL, C. R., SUMER, B. M. & FREDSØE, J. 1998 Turbulent combined oscillatory flow and current in a pipe. *J. Fluid Mech.* **373**, 313–348.

LUCHINI, P. & BOTTARO, A. 2001 Linear stability and receptivity analyses of the Stokes layer produced by an impulsively started plate. *Phys. Fluids* **13**, 1668–1678.

LUO, J. & WU, X. 2004 Influence of small imperfections on the stability of plane poiseuille flow: a theoretical model and direct numerical simulation. *Phys. Fluids* **16**, 2852–2863.

MERKLI, P. & THOMANN, H. 1975 Transition to turbulence in oscillating pipe flow. *J. Fluid Mech.* **68**, 567–576.

MONKEWITZ, A. 1983 Lineare stabilitats untersuchungen an den aszillierenden grenzschichten von Stokes. PhD thesis 7297, Stabilitaets, Oszillierenden, Federal Institute of Technology, Zurich.

NEREM, R. M., SEED, W. A. & WOOD, N. B. 1972 An experimental study of the velocity distribution and transition to turbulence in the aorta. *J. Fluid Mech.* **52**, 137–160.

OJHA, M., COBBOLD, R. S. C., JOHNSTON, K. W. & HUMMEL, R. L. 1989 Pulsatile flow through constricted tubes: an experimental investigation using photochromic tracer method. *J. Fluid Mech.* **203**, 173–197.

ORLANDI, P. 2000 *Fluid Flow Phenomena: A Numerical Toolkit*. Kluwer.

PEDLEY, T. 1980 *The Fluid Mechanics of Large Blood Vessels*. Cambridge University Press.

POPE, S. B. 2000 *Turbulent Flows*. Cambridge University Press.

RAI, M. M. & MOIN, P. 1991 Direct simulations of turbulent flow using finite-difference schemes. *J. Comput. Phys.* **96**, 15–53.

RAMAPRIAN, B. R. & TU, S. 1980 An experimental study of oscillatory pipe flow at transitional Reynolds numbers. *J. Fluid Mech.* **100**, 513–544.

SARPKAYA, T. 1966 Experimental determination of the critical Reynolds number for pulsating Poiseuille flow. *Trans. ASME* D: *J. Basic Engng* **88**, 589–598.

SERGEEV, S. I. 1966 Fluid oscillations in pipes at moderate reynolds number. *Fluid Dyn. (Merkh. Zh.)* **1**, 21–22.

SHEMER, L., WYGNANSKI, I. & KIT, E. 1985 Pulsating flow in a pipe. *J. Fluid Mech.* **153**, 313–337.

SPALART, P. M. & BALDWIN, B. S. 1987 Direct simulation of a turbulent oscillating boundary layer. In *Symp. on Turbulent Shear Flows, Toulouse, 7–9 September* (ed. F. S. F. Durst, B. Launder & J. Whitelaw).

STETTLER, J. C. & HUSSAIN, A. K. M. F. 1986 On transition of the pulsatile pipe flow. *J. Fluid Mech.* **170**, 169–197.

TROMANS, P. 1976 The stability of oscillatory pipe flow. abstract of lecture given at Euromech 73: *Oscillatory Flows in Ducts, Aix-en-Provence, April 13–15.*

TUZI, R. 2006 Transition in oscillatory and pulsating pipe flows. PhD thesis, Department of Environmental Engineering, University of Genova, Italy.

VERZICCO, R. & VITTORI, G. 1996 Direct simulation of transition in a Stokes boundary layer. *Phys. Fluids* **8**, 1341–1343.

VITTORI, G. & VERZICCO, R. 1998 Direct simulation o transition in an oscillatory boundary layer. *J. Fluid Mech.* **371**, 207–232.

VON KERCZEK, C. & DAVIS, S. H. 1974 Linear stability theory of oscillatory Stokes layers. *J. Fluid Mech.* **62**, 753–773.

WU, X. 1992 The nonlinear evolution of high-frequency resonant-triad waves in an oscillatory Stokes layer at high Reynolds number. *J. Fluid Mech.* **245**, 553–597.

WU, X. & LUO, J. 2006 Influence of small imperfections on the stability of plane Poiseuille flow and the limitation of Squire's theorem. *Phys. Fluids* **18**, 044104–1–14.

YELLIN, E. L. 1966 Laminar-turbulent transition process in pulsatile flow. *Circulation Res.* **19**, 791–804.